

Development of Analysis Techniques for Dynamic Magnetic Resonance Imaging of the Knee

– Master Thesis –

to be awarded

Master of Science in Medical Photonics

submitted by

Aayush Nepal

May 28, 2024

Aayush Nepal
aayush.nepal@uni-jena.de
Student ID: 198683

Supervisor

1st: Prof. Dr. rer. nat. med. habil. Jürgen Reichenbach
2nd: Dr. rer. nat. Martin Krämer

Friedrich-Schiller-Universität Jena
Medizinischen Fakultät
Institut für Diagnostische und Interventionelle Radiologie
Philosophenweg 3
07743 Jena

Abstract

The knee joint, a critical component of human movement, frequently endures mechanical loads that can lead to degenerative conditions such as osteoarthritis (OA). OA, prevalent globally and particularly affecting the knee, demands early diagnosis for effective intervention. Magnetic resonance imaging (MRI) has proven effective in detecting soft tissue changes, but traditional MRI studies often miss early-stage OA indicators as they are conducted under non-weight-bearing conditions, unlike the actual physiological state during daily activities.

This thesis leverages recent advancements in MRI technology to analyze the knee joint under mechanical loading, using high-resolution CINE MRI imaging. This approach enables the investigation of dynamic interactions between the femur and tibia during flexion-extension cycles, providing detailed insights into knee mechanics. A major challenge in this process is the accurate segmentation of anatomical structures, critical for reliable biomechanical measurements. To address this, a semi-automated segmentation pipeline was developed, streamlining the process and improving consistency across sequential images.

Following segmentation, the study quantified biomechanical parameters, such as the angle between the long axes of the femur and tibia and the distance between anatomical landmarks, under various loading conditions. The results showed significant variations in distance measurements during the early phase of flexion, highlighting the knee's sensitivity to external loading. However, no significant differences were found in the angular measurements, suggesting stability in bone alignment under load.

This research demonstrates the potential of semi-automated segmentation for efficient and precise analysis of dynamic knee MRI scans, offering significant advantages for clinical and research applications. Despite the promising findings, the study's reliance on single 2D slices limits the comprehensive assessment of knee kinematics. Future work should extend this methodology to 3D analyses and explore its application to patellofemoral kinematics, providing a more holistic understanding of knee mechanics.

In conclusion, this thesis presents a robust method for analyzing knee joint biomechanics using advanced MRI techniques, paving the way for enhanced diagnostic and research capabilities in orthopedics.

Acknowledgements

Contents

List of Figures	v
List of Tables	viii
List of Acronyms	ix
1 Introduction	1
2 Fundamentals	3
2.1 The Knee Joint	3
2.2 Dynamic MRI	7
2.2.1 CINE imaging	7
2.2.2 Gating	8
2.2.3 Knee loading device	8
2.2.4 Gradient Echo FLASH sequence	11
2.2.5 Radial golden-angle acquisition	14
3 Methodology	17
3.1 Data Collection Methods	17
3.1.1 Procedure Details	17
3.1.2 Sequence Parameters and Reconstruction	18
3.2 Data Analysis	21
3.2.1 Segmentation	21
3.2.2 Extraction of Biomechanical Parameters	29
4 Results	32
4.1 Edge tracking and segmentation	32
4.2 Biomechanical parameter extraction	34
5 Discussion	36
5.1 Edge tracking and segmentation	37
5.2 Angle calculation	38
5.3 Distance calculation	39
6 Conclusion	40

References	43
A Appendix	48

List of Figures

1	Anatomy of the right knee joint showing bones, cartilage, and ligaments. Left: front view; Right: side view. Key structures include the femur (thigh bone), tibia (shinbone), fibula (calf bone), patella (kneecap), articular cartilage, meniscus, and various ligaments such as the cruciate ligaments, lateral collateral ligament, and medial collateral ligament. (IQWiG 2021)	3
2	Anterior (top, showing the knee in flexion) and posterior (bottom, showing the knee in extension) views of the right knee, with labeled articular surfaces of the medial and lateral condyles. [Edited] (Netter 2023, p.519)	4
3	Right knee joint opened, with the knee in a slightly flexed position, exposing the articular surface of the patella.[Edited] (Netter 2023, p.517)	5
4	The knee joint motion in three dimensions, described using six degrees of freedom: anterior/posterior translation, medial/lateral shift, compression/distraction, abduction/adduction, flexion/extension, and medial/lateral rotation. The arrows indicate the direction of each movement. (Standring and Gray 2021, p. 1412).	6
5	The MR330 controller (left) and MR338 optical fiber position sensor system (right), connected via duplex LC multimode fiber optic cabling, with a maximum distance of up to 300 meters. The setup illustrates the separation between the outside MRI area and the MRI-safe area.	9
6	The redlab I/O module.	9
7	Noras Variety 16 channel flex coils, designed for MRI applications. The image shows the flex coil with a central square exterior featuring Velcro for secure strapping, highlighting its flexible design	10
8	”A 3D rendering of the knee motion/loading device (left) and two photographs of the device in a Siemens Magnetom Prisma Fit MRI scanner (right). The top right image (rear view) demonstrates how the distal part of the device sits atop the rails within the scanner bore, which are normally used to guide and support the patient table. The bottom right image (front, oblique view) demonstrates an individual positioned in the device with a flexible coil around the index knee, the thigh secured between the proximal pillow blocks and the ankle fastened to the leg support, as well as the coil plug setup” (Brisson, Krämer, et al. 2022).	10

9	FLASH sequence diagram. The diagram illustrates the key components of the FLASH sequence: RF Pulse (α°), Slice-Selecting Gradient (G_{SS}), Phase Encoding Gradient (G_{PE}), Frequency Encoding Gradient (G_{FE}), Signal, and Spoiler Gradient, echo time (TE) and repetition time (TR)	14
10	Generic radial k-space sampling diagram. The image shows concentric circles representing constant k-space radii, with k_x and k_y axes indicating spatial frequencies. The lines labeled '1st line' and '2nd line' demonstrate different radial sampling lines, each separated by an angle $\Delta\theta$. The equation $\Delta k_\theta = k_{\max} \Delta\theta$ illustrates that the change in the k-space coordinates along a specific angular direction (Δk_θ) is proportional to the maximum k-space radius (k_{\max}), which determines the highest spatial frequency sampled, and the angular step size ($\Delta\theta$). (Brown, Cheng, et al. 2014, p.306)	15
11	Radial k-space sampling strategies. (a) Fixed angular increment ($\phi = 180^\circ/10$), showing potential for uneven k-space coverage. (b) Golden-angle sampling ($\phi_{GR} = 111.25^\circ$), ensuring uniform distribution across k-space as the number of projections (P) increases (Winkelmann, Schaeffter, et al. 2007).	16
12	Left: Exemplary k-space data acquired during a specific frame of the knee flexion cycle. Right: Reconstructed MRI image in real space obtained by applying an inverse 2D Fast Fourier Transform (2D IFFT) to the k-space data	17
13	Output of the Canny edge detection algorithm applied to one of the frames, showing the detected edges of the tibia and femur bones overlaid on top of the original image for visual comparison.	22
14	Output from the labeling algorithm with the representative edges for femur (top) and tibia(bottom) highlighted. Distinct colors represent a different label identified by the labeling algorithm.	24
15	A zoomed in look at the equidistant sampled points (orange) along the boundary of the tibia edge (white).	26
16	Left: The reference points in the first frame (orange) overlaid with the binary edge image of the target frame (white).Right: The reference points have been transformed by using the results from the optimization showing almost perfect overlap, illustrating the effective alignment achieved through the minimization of the cost function.	28
17	Manual segmentation is performed to complete the boundary of the tibia's interior edge shown in green, along with the reference points (orange).	29
18	The long axis of the bones are identified by using the PCA (blue) along with the centroid (white cross) for each segment. θ represents the angle that is being measured	31

19	Points based on anatomical landmarks are shown in yellow.	32
20	Mean alignment error per point across all frames for each tibia dataset.	33
21	A mosaic showing the segmented tibia and femur shapes(green) where each tile is a particular time point. The leg is fully flexed at Frame 0	33
22	Plot of angle between long axes of bone segments between tibia and femur versus the flexion percentage.The x-axis ticks represent the centers of bins, each with a width of 10 percentage units. The shaded regions represent one standard deviation uncertainty. Angles greater than 180° imply hyperextension.	35
23	Plot showing the variation of euclidean distance between two points with across time in the motion cycle. All distances are relative to the baseline measurement at -100% flexion, set at 0 mm. The shaded region represents one standard deviation uncertainty.	36
24	Femur (a) and tibia (b) shaft axes defined in CT and T1-weighted MRI scans in the sagital view. (Dai, Sha, et al. 2021)	39
25	Non aggregated results for the angle between the long axis of the bone segments. Loaded and unloaded measurements are shown in their respective columns.	48
26	Non aggregated results for the euclidean distance between anatomical landmarks on the femur and tibia. Loaded and Unloaded conditions are shown in their respective columns.	48

List of Tables

1	Range of Motion for Different Datasets	18
2	MRI Sequence Parameters	19

List of Acronyms

ADMM	Alternating Direction Method of Multipliers
Cov	Covariance matrix
FLASH	Fast Low Angle Shot
FoV	Field of View
GRE	Gradient Echo
MRI	Magnetic Resonance Imaging
OA	Osteoarthritis
PCA	Principal Component Analysis
SHM	Screw Home Mechanism
TE	Time to Echo
TGV	Total Generalized Variation

1 Introduction

The knee joint, a crucial structure in human movement, consists of various tissues with distinct structural and mechanical properties, including articular cartilage and meniscus. These components are regularly subjected to compressive mechanical loads, making them susceptible to degenerative conditions such as osteoarthritis (OA). OA affects a significant portion of the global population and the knee joint is among its common targets, leading to functional impairments and increased health-care costs. ([WHO 2023](#)) A comprehensive survey across 15 European countries and Israel found that knee pain was the third most commonly reported type of chronic pain, underscoring the significant public health concern it represents (Breivik, Collett, et al. [2006](#)). Furthermore, OA was identified as the most common cause of this pain. This situation has not improved over time. In Germany, for instance, a recent retrospective study found that the number of patients with OA is steadily rising (Obermüller, Jerosch, et al. [2024](#)). As society ages, the prevalence and impact of OA are expected to rise, posing significant public health challenges. (Yelin, Weinstein, and King [2016](#)). Knee-related issues are prevalent and impactful due to the inherent complexity of the knee joint itself. As a hub of various anatomical structures working in unison, the knee supports a range of movements and bears significant loads, making it susceptible to a variety of injuries and conditions. Early diagnosis of OA is crucial for timely intervention, and understanding the anatomy of the knee is the first step in tackling this problem. Magnetic resonance imaging (MRI) has emerged as a promising non-invasive technique for early diagnosis of OA due to its excellent soft tissue contrast and high spatial resolution (Kijowski, Demehri, et al. [2020](#)).

Traditionally, MRI studies aimed at assessing the structure and function of the knee joint have been performed with the joint at rest or in non-weight-bearing conditions, which, however, do not accurately reflect the physiological state of the knee during daily activities (Blankevoort, Huiskes, and De Lange [1988](#)). For instance, research has shown that bone marrow lesions, which are associated with osteoarthritis progression, are significantly related to mechanical loading during activities like walking, highlighting the limitations of non-weight-bearing MRIs in detecting early-stage OA (Bennell, Creaby, et al. [2010](#)). Additionally, dynamic MRI studies have demonstrated that knee kinematics during continuous movement reveal significant differences compared to static positions, providing crucial information that static scans may miss (d'Entremont, Nordmeyer-Massner, et al. [2013](#)).

Recent advancements in MRI technology have enabled the study of knee joints under mechanical loading conditions, better mimicking the actual physiological environment by allowing both controlled application of loads and dynamic movement during imaging (Brisson, Oliveira, et al. 2024) (Conconi, De Carli, et al. 2023) (Jogi, Thaha, et al. 2022). MRI-compatible loading devices facilitate the investigation of how tissues deform and how their morphology changes in response to stress and movement. Various MRI measures, including tissue deformation from magnitude images, phase information, and quantitative MRI, have been employed to assess these changes.

Building on these recent advancements in MRI technology, this thesis utilizes high-resolution dynamic MRI to develop a method for analyzing the relative movements between the femur and tibia during flexion-extension cycles under various loading conditions. This method is then applied to track specific kinematic parameters at various points in the movement cycles, providing a basis for validating the method and conducting detailed biomechanical analyses.

To achieve reliable kinematic analyses, the initial step involves accurately segmenting key anatomical structures from the dynamic MRI sequences. This segmentation is crucial, as it significantly influences the reliability of biomechanical measurements derived from the MRI data. Traditionally, segmentation of musculoskeletal tissues has been performed manually in which a user delineates the boundaries of each joint structure on each MR image slice that is extremely time-consuming with its efficiency and repeatability influenced by the level of user expertise. (McWalter, Wirth, et al. 2005). This problem is exacerbated when dealing with multiple frames in a dynamic sequence. On the other hand, modern techniques like Convolutional Neural Networks (CNNs) and U-Nets are being widely used to automate the segmentation process (Liu, Zhou, et al. 2018). Unfortunately, these methods typically require large annotated datasets for training, which are not available for the type of dynamic frames in this project. To address these issues, this thesis proposes the development of a semi-automated pipeline to segment the tibia and femur from the dynamic MRI data, specifically from single-slice 2D images in sagittal view captured throughout the knee's motion cycle under both loaded and unloaded conditions. This new methodology aims to streamline the segmentation process, reducing the time and effort involved while enhancing accuracy and consistency across sequential images.

Following the successful segmentation of the bones, the subsequent analysis involves quantifying two distinct biomechanical parameters: the angle between the long axes of the tibia and femur segments and the distance between specific anatomical landmarks on these bones. These parameters were chosen because they naturally capture

the relative motion and spatial relationships between the femur and tibia, which are essential for understanding knee joint mechanics. The purpose of this quantification is to investigate how these parameters change throughout the motion cycle and how they vary under loaded and unloaded conditions. Conducting this study on healthy volunteers aims to establish normative trends that can serve as benchmarks for future comparisons with patient data, potentially aiding in the assessment of knee joint stability and functionality.

2 Fundamentals

2.1 The Knee Joint

The knee joint is the largest and the most superficial synovial joint in the body (Dalley, Agur, and Moore 2023). The anatomy of the knee joint includes several important structures such as bones, cartilage, and ligaments. These components work together to provide stability and flexibility to the joint. Figure 1 illustrates the anatomy of the right knee joint, highlighting these key structures.

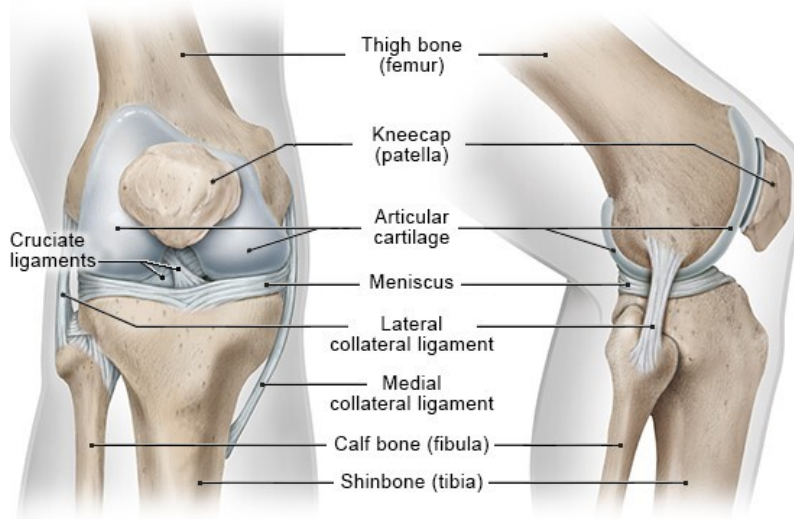


Figure 1: Anatomy of the right knee joint showing bones, cartilage, and ligaments. Left: front view; Right: side view. Key structures include the femur (thigh bone), tibia (shinbone), fibula (calf bone), patella (kneecap), articular cartilage, meniscus, and various ligaments such as the cruciate ligaments, lateral collateral ligament, and medial collateral ligament. (IQWiG 2021)

It consists of three compartments that form a dynamic, specialized hinge joint (Standring and Gray 2021, p.1395). These compartments are the medial compartment, the lateral compartment, and the patellofemoral compartment. Each compartment contains primary articulations that contribute to the joint's biomechanical performance. Specifically, the knee comprises two femorotibial articulations—one in the medial compartment and one in the lateral compartment (see Figure 2)—and one femoropatellar articulation in the patellofemoral compartment (see Figure 3). These articulations, illustrated in are defined by their complexity and incongruence.

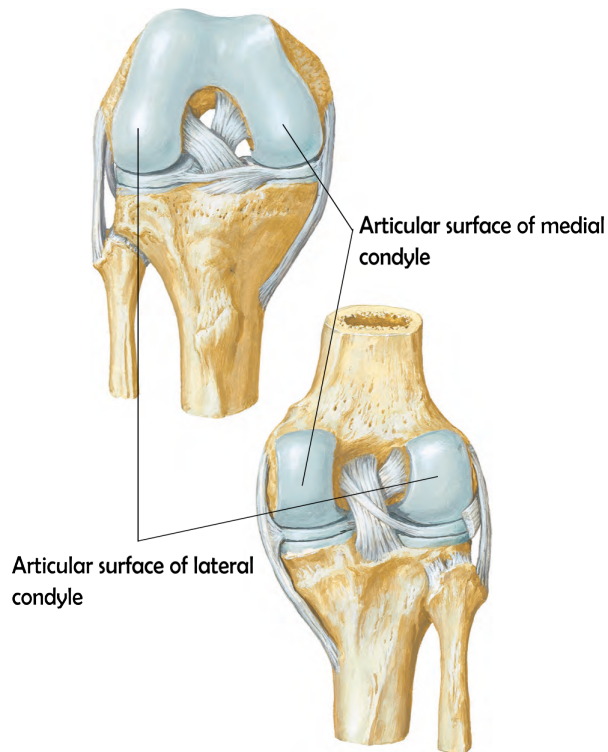


Figure 2: Anterior (top, showing the knee in flexion) and posterior (bottom, showing the knee in extension) views of the right knee, with labeled articular surfaces of the medial and lateral condyles. [Edited] (Netter 2023, p.519)

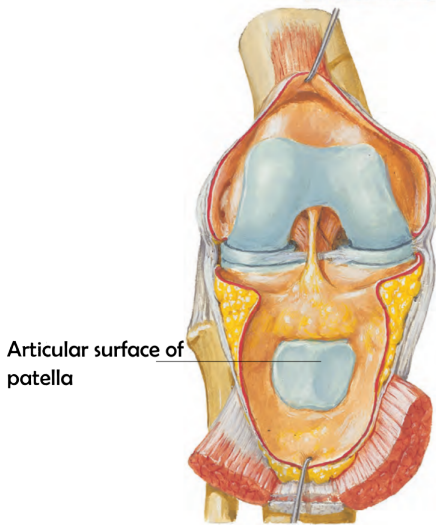


Figure 3: Right knee joint opened, with the knee in a slightly flexed position, exposing the articular surface of the patella.[Edited] (Netter 2023, p.517)

This design allows the knee to manage a wide array of movements and bear significant loads. Figure 4 illustrates the knee's capacity for multidimensional movement, highlighting the joint's sophisticated structural design that enables this versatility. However, this inherent design also renders the knee vulnerable to a range of forces, including compressive forces acting on bone and cartilage, tensile stresses in peri-articular ligaments, and substantial muscular forces required to maintain balance during weight-bearing activities. (Standring and Gray 2021) For instance, during symmetrical stance on both feet, each knee supports approximately 43 % of the body's weight, necessitating precise muscular coordination to maintain equilibrium (Maquet 2012).

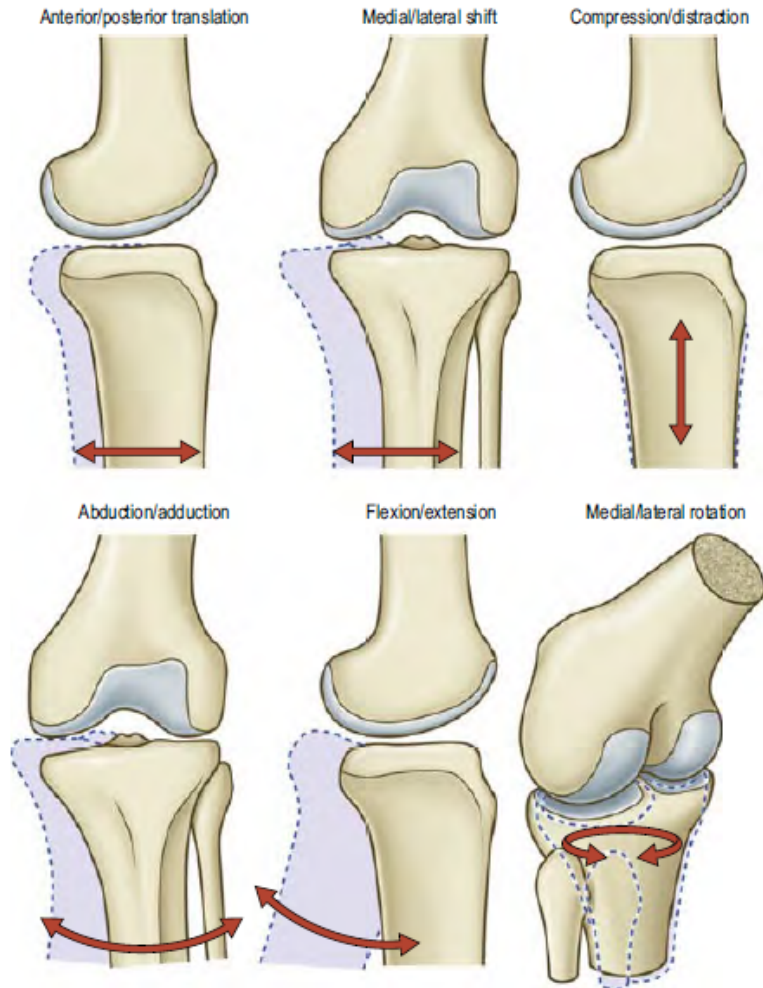


Figure 4: The knee joint motion in three dimensions, described using six degrees of freedom: anterior/posterior translation, medial/lateral shift, compression/distraction, abduction/adduction, flexion/extension, and medial/lateral rotation. The arrows indicate the direction of each movement. (Standring and Gray 2021, p. 1412).

Such mechanical forces, influenced by activities and body mass index (BMI), are significant causes of OA and represent one of the most modifiable risk factors (Heidari 2011). Both static and dynamic forces play critical roles in the pathophysiology of OA. Static forces, such as those experienced while standing, contribute significantly to mechanical stress on the knee joint, exacerbating the risk of OA (Egloff, Hügle, and Valderrabano 2012). Additionally, abnormal joint loading during movement is a key mechanical driver of osteochondral changes that contribute to the initiation and progression of knee OA (Coburn, Crossley, et al. 2023).

The relationship between biomechanical stresses and knee health highlights the need for diagnostic tools that fulfill two key criteria: they must capture the knee's dynamic behavior during motion and assess the joint under varying loads. Dynamic MRI is emerging as a notable imaging modality that meets these criteria (Conconi, De Carli, et al. 2023).

2.2 Dynamic MRI

In a broad sense, dynamic MRI is an umbrella term encompassing various MRI techniques designed to capture and visualize physiological processes and motion over time. The dynamic aspect of MRI is crucial for studying systems or structures involving inherent motion, such as blood flow, tissue perfusion, or cardiac activity. For the purposes of this project, the focus of "dynamic MRI" narrows down to capturing the bulk movement of the knee joint undergoing active flexion extension cycles inside the scanner. Compared to traditional static MRI scans, which are highly susceptible to motion artifacts compared to other imaging modalities (Zaitsev, Maclarens, and Herbst 2015), dynamic MRI techniques not only accommodates motion, but can even leverage it to offer comprehensive insights into the functional and biomechanical properties of the concerned structures. Among these techniques, CINE imaging, particularly renowned in cardiac MRI, is considered the gold standard for evaluating cardiac function (Menchón-Lara, Simmross-Wattenberg, et al. 2019). Its high regard in cardiac MRI demonstrates the method's precision and adaptability—traits that are leveraged in knee imaging.

2.2.1 CINE imaging

CINE, derived from 'cinematography,' refers to creating a movie-like sequence of images. In the context of dynamic knee MRI, this technique can be used to reconstruct a "movie" of a single flexion-extension cycle. This visualization is achieved by aggregating multiple partial datasets acquired over various cycles. The knee's movement cycle is segmented into distinct stages, each corresponding to a specific angle of flexion or extension. For each stage, k-space — the Fourier transform space from which MR images are reconstructed — is incrementally sampled. This data is gathered across multiple repetitions of the movement cycle, ensuring comprehensive coverage of k-space and thus, high-resolution imaging of each movement phase. This technique works robustly only if the movement cycles of the knee during imaging

are sufficiently similar to each other (Curtis and Cheng 2022). Achieving this consistency in dynamic MRI of the knee, which naturally involves significant movement variations, requires precise synchronization of the imaging process with the knee’s motion cycle.

2.2.2 Gating

This synchronization, known as gating, aligns image acquisition with specific, repeatable points in the knee’s movement cycle. By ensuring each captured image corresponds accurately to a consistent phase of motion, it minimizes the discrepancies that can arise from cycle-to-cycle variations, enhancing the reliability of bio-mechanical analyses. There are two main types of gating: retrospective and prospective. In prospective gating, image acquisition is triggered at specific points in the motion cycle in real-time. In retrospective gating, the data is acquired continuously throughout the motion cycle (Edelman 2005). The data is then reordered post-acquisition into a coherent sequence that captures the knee at different positions along the motion cycle. This necessitates external information that captures the precise moment and position of the knee throughout its range of movement beyond just the raw data acquired during the MRI scan. A MR-safe knee loading device is employed to address this, which comes with an optical sensor attachment that provides this vital information that includes the exact timing and degree of knee flexion and extension, which is essential for accurately synchronizing the imaging frames with specific phases of the knee’s motion cycle (Brisson, Krämer, et al. 2022).

2.2.3 Knee loading device

The MR-compatible knee loading device employed in this study is illustrated in Figure 8. This device allowed for a range of motion of approximately 25 to 45 degrees (subject-dependent), enabling subjects to perform knee flexion and extension cycles under both loaded and unloaded conditions. For loading, the device was equipped with compartments for weight plates and sandbags, providing a physiological load of 10 to 12 kilograms. These weights are positioned at the end of the device near the subject’s lower limb. As the subject extends the leg, they must overcome not only the natural resistance of their body weight but also the additional external load imposed by these weights. Similarly, as the subject flexes the leg from the extended position, they have to lower the leg in a controlled manner. Central to this

device's functionality is an optical fiber position sensor (MR338-Y10C10, Micronor, 155 Camarillo, CA, USA), which precisely measures the absolute angle from 0° to 360° with a resolution of 0.025° (Rickenbach 2013). This measurement capability is critical for synchronizing the knee's movement with MRI data reconstruction.

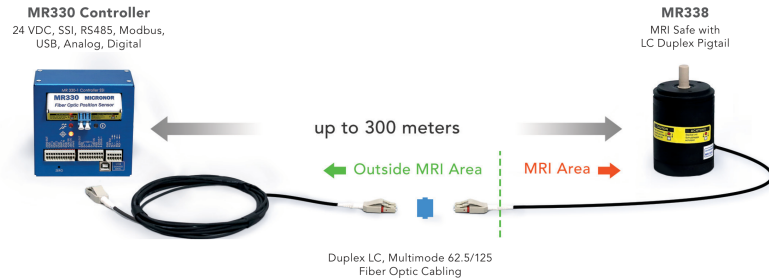


Figure 5: The MR330 controller (left) and MR338 optical fiber position sensor system (right), connected via duplex LC multimode fiber optic cabling, with a maximum distance of up to 300 meters. The setup illustrates the separation between the outside MRI area and the MRI-safe area.

As shown in Figure 5 , the MR330 controller interfaces with the MRI-safe MR338 position sensor to facilitate precise measurement within the MRI environment, accommodating up to 300 meters of fiber optic cabling. The controller is connected to a acquisition computer placed outside the scanner while the sensor is attached to the device within. The MR338 rotary encoder continuously monitors the knee's rotation angle using optical signals, which are converted into electrical signals by the MR330 controller. These electrical signals are then sent to the RedLab 1208LS, a USB-based data acquisition module designed for measuring and controlling analog and digital signals (refer to Figure 6). The MRI scanner outputs trigger signals for each sequence repetition, which are also captured by the RedLab 1208FS-Plus. Both the knee rotation signals and the trigger signals are simultaneously sampled by the RedLab 1208FS-Plus and then transmitted to the acquisition computer via USB. The acquisition computer converts these signals into binary data, which is later used for reconstructing the synchronized knee motion and MRI imaging data.



Figure 6: The redlab I/O module.

To enhance signal acquisition and the clarity of imaging, two flexible coils (Noras, Variety) as shown in Figure 7 were positioned at key anatomical locations: one at the distal femur and another at the proximal tibia, as specified in the MRI protocol.

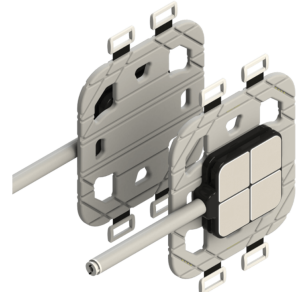


Figure 7: Noras Variety 16 channel flex coils, designed for MRI applications. The image shows the flex coil with a central square exterior featuring Velcro for secure strapping, highlighting its flexible design

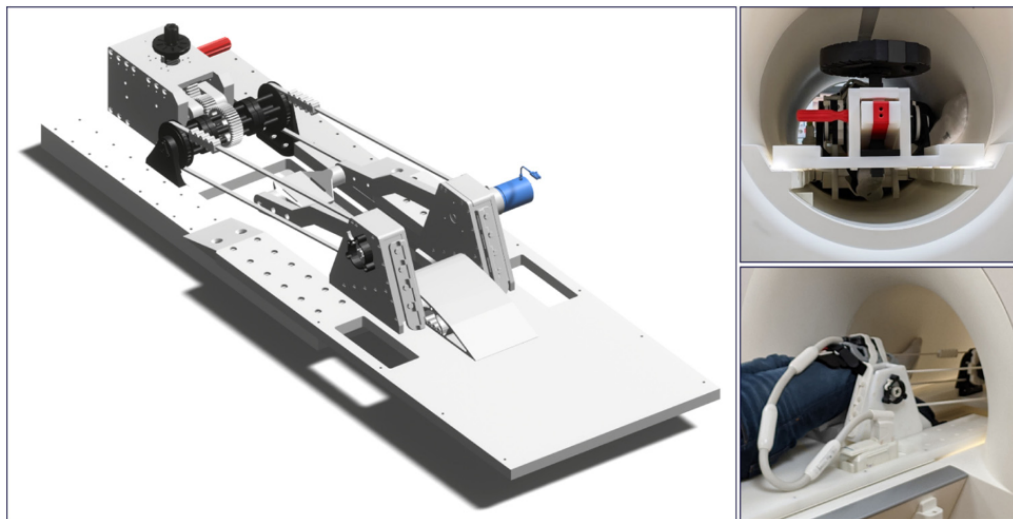


Figure 8: ”A 3D rendering of the knee motion/loading device (left) and two photographs of the device in a Siemens Magnetom Prisma Fit MRI scanner (right). The top right image (rear view) demonstrates how the distal part of the device sits atop the rails within the scanner bore, which are normally used to guide and support the patient table. The bottom right image (front, oblique view) demonstrates an individual positioned in the device with a flexible coil around the index knee, the thigh secured between the proximal pillow blocks and the ankle fastened to the leg support, as well as the coil plug setup” (Brisson, Krämer, et al. 2022).

To further enhance the quality and precision of the imaging, and to maximize the potential for precise image reconstruction, a previously reported radial golden-angle

gradient-echo Fast Low-Angle Shot (FLASH) sequence was used, which is more robust against motion artifacts than Cartesian sequences (Aleksiev, Krämer, et al. 2022). The following sections will detail the key components of this technique — radial golden-angle acquisition and the gradient-echo FLASH sequence.

2.2.4 Gradient Echo FLASH sequence

Basics

At its core, MRI is an imaging technique based on the interaction of nuclear spins with an external magnetic field (B_0). The primary nucleus used in MRI is the proton in hydrogen, which precesses around the direction of this external field. When placed in the magnetic field, these protons align with or against the direction of B_0 , creating a net magnetization vector M_z along the field direction. Imaging the human body relies on manipulating and detecting the bulk precession of these hydrogen spins in water, fat, and other organic molecules. (Brown, Cheng, et al. 2014). This manipulation is achieved through various sequences of magnetic field gradients, radiofrequency pulses, and timing sequences.

One such commonly used sequence is the gradient echo (GRE) sequence. Like any other sequence, the process begins with the application of a radiofrequency (RF) pulse. This RF pulse is an oscillating magnetic field applied at the Larmor frequency, which is the natural precession frequency of the hydrogen protons in the magnetic field. This frequency ω_0 is given by the Larmor equation:

$$\omega_0 = \gamma B_0 \quad (1)$$

where γ is the gyromagnetic ratio and B_0 is the external magnetic field. When the frequency of the RF pulse matches the Larmor frequency, it resonates with the protons, causing the net magnetization vector (M_z) to tip from the longitudinal axis into the transverse plane, creating transverse magnetization (M_{xy}). This is where the term "resonance" in Magnetic Resonance Imaging originates.

M_{xy} generates the detectable MRI signal by inducing an oscillating voltage in the receiver coils, which is known as free induction decay (FID). However, to form a meaningful image, it is essential to encode spatial information within this signal. This spatial encoding is achieved through the use of gradient magnetic fields applied in various directions. These gradients alter the precession frequencies of the protons

based on their spatial positions, allowing the MRI system to map the location of the signals within the body.

The three gradient fields

The first gradient field applied is the slice-selecting gradient (G_{SS}). It is applied in the direction of (B_0), simultaneously with the application of the RF pulse. This gradient varies the magnetic field strength along the z-axis, causing the protons to precess at different frequencies according to equation 1. As a result, only the protons at a specific location along the z-axis, where their Larmor frequency matches the RF pulse frequency, will resonate and be tipped into the transverse plane, thereby selecting a specific slice for imaging. Immediately after the RF pulse and G_{SS} , a rephasing gradient with opposite polarity in the slice-selecting direction is applied. The purpose of this rephasing lobe is to correct for any dephasing caused by the initial G_{SS} . When the initial gradient is applied, protons within the selected slice experience slightly different magnetic field strengths, causing them to dephase. The rephasing gradient lobe reverses this effect by applying a gradient of the same magnitude but opposite polarity, bringing the spins back into phase within the selected slice. This ensures that M_{xy} is coherent, maximizing the strength of the detectable signal.

Once the slice is selected, along two perpendicular directions in the transverse plane must be performed. The process begins with frequency encoding. Another gradient field, lets say in the x-direction, called the frequency encoding gradient (G_{FE}), is applied simultaneously during signal acquisition. When this gradient is applied, protons experience different precession frequencies based on their spatial location along the x-axis. The sampled signal will be a superposition of these frequencies, which can be resolved by performing an inverse Fourier transform (FFT) to reconstruct the spatial information along the x-direction. Before the main G_{FE} is applied during acquisition, a gradient of opposite polarity, known as the prephasing gradient, is briefly applied. This prephasing gradient slightly dephases the spins, establishing a known initial phase relationship. When the main frequency encoding gradient is subsequently applied, it causes the spins to rephase, forming an echo signal at a specific time. This rephasing process generates the "gradient echo," which is the reason for naming this sequence as it is. The prephasing gradient is typically shorter and is followed by the longer main frequency encoding gradient, ensuring that the spins are coherently rephased at the start of signal acquisition, maximizing the strength of the detected signal.

Next, phase encoding is performed to spatially encode information along the second perpendicular (y) direction. The phase encoding gradient (G_{PE}) is briefly turned on and then off before G_{FE} is applied. During the time G_{PE} is on, the spins start precessing at different frequencies based on their spatial location along the y-axis, causing them to dephase. When G_{PE} is turned off, the spins return to precessing at the Larmor frequency, but the phase differences induced by the gradient remain.

After this initial encoding, the same sequence is repeated multiple times. Each repetition is identical except for the magnitude of the phase encoding gradient G_{PE} , which is varied systematically. By altering the strength of G_{PE} in each repetition, different phase shifts are induced, corresponding to different spatial locations along the y-axis. This process effectively samples the spatial information across the entire y-direction. The collected data from these repetitions fill what is known as k-space, a matrix that represents the spatial frequency domain of the image. Each line in k-space corresponds to a different phase encoding step. Once k-space is fully sampled, an inverse Fourier transform (FFT) is performed to convert the frequency-domain data into a spatial-domain image. This combination of frequency encoding and phase encoding allows for the reconstruction of a two-dimensional image of the selected slice.

FLASH

The refocusing gradient used in gradient-echo pulse sequences allows for significantly shorter echo times (TE), facilitating faster imaging (Westbrook and Talbot 2019, p.94). However, certain applications, such as dynamic MRI of moving body parts like the leg, demand even quicker acquisition times. To meet these demands, the Fast Low Angle Shot (FLASH) GRE sequence was developed (Haase, Frahm, et al. 1986). FLASH employs low flip angle RF pulses, which reduce the time needed for the longitudinal magnetization to recover, thereby shortening the repetition time (TR).

Another important aspect of FLASH sequences is the management of residual transverse magnetization. In gradient echo sequences, after a series of RF pulses, the system reaches a condition known as the steady state. In this state, the magnitude of M_z remains consistent at the end of each TR. However, there can also be residual M_{xy} at the start of each repetition cycle. If this residual transverse magnetization is not managed, it can interfere with the signal and degrade image quality. To address this, FLASH sequences incorporate a strong spoiler gradient in the slice-selecting direction. This gradient deliberately dephases the residual transverse magnetiza-

tion, ensuring that it does not contribute to the signal in subsequent cycles. By effectively "spoiling" the transverse magnetization, the sequence starts fresh with each repetition, reducing artifacts and enhancing image clarity.

A typical FLASH sequence diagram is shown in Figure 9, illustrating the application of low flip angle RF pulses, frequency encoding gradients, and the spoiler gradient.

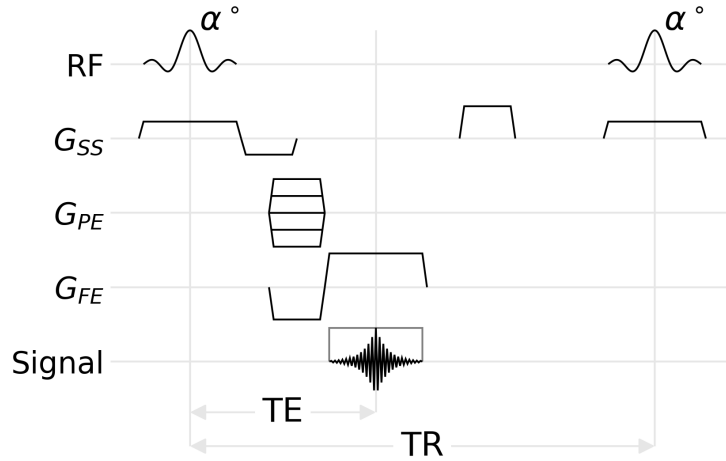


Figure 9: FLASH sequence diagram. The diagram illustrates the key components of the FLASH sequence: RF Pulse (α°), Slice-Selecting Gradient (G_{SS}), Phase Encoding Gradient (G_{PE}), Frequency Encoding Gradient (G_{FE}), Signal, and Spoiler Gradient, echo time (TE) and repetition time (TR)

2.2.5 Radial golden-angle acquisition

As the name suggests, radial golden-angle acquisition specifically modifies how k-space is sampled. Unlike traditional static MRI, which typically employs Cartesian line by line sampling, this method utilizes radial sampling. Here, the data points are collected along radial lines spreading out from the center of k-space, resembling spokes on a wheel. Figure 10 depicts a generic radial sampling scheme. The separation between any two adjacent circles defines the separation Δk_r in the radial sampling direction, whereas, the angular separation between any two successive angular lines in k-space (such as between the two example lines shown in the figure) defines $\Delta\theta$. The two quantities Δk_r and $\Delta\theta$ are constrained by the Nyquist sampling criterion. (Brown, Cheng, et al. 2014)

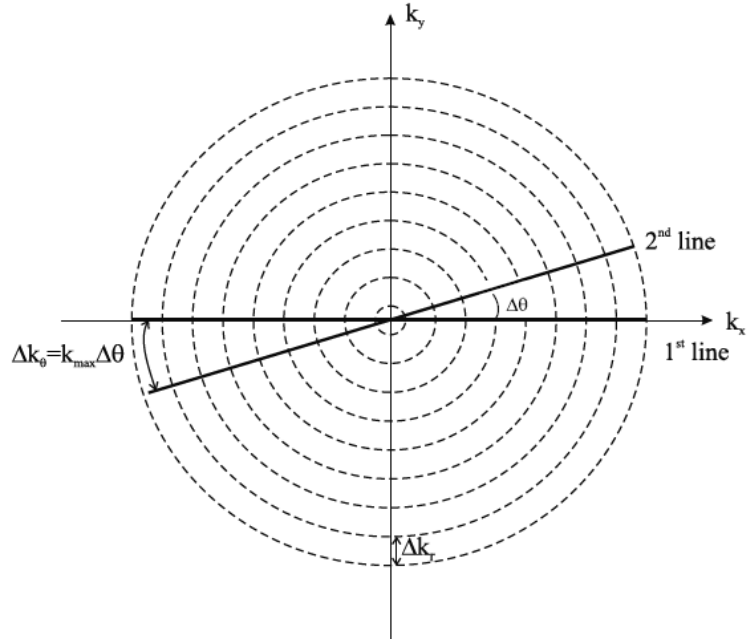


Figure 10: Generic radial k-space sampling diagram. The image shows concentric circles representing constant k-space radii, with k_x and k_y axes indicating spatial frequencies. The lines labeled '1st line' and '2nd line' demonstrate different radial sampling lines, each separated by an angle $\Delta\theta$. The equation $\Delta k_\theta = k_{\max} \Delta\theta$ illustrates that the change in the k-space coordinates along a specific angular direction (Δk_θ) is proportional to the maximum k-space radius (k_{\max}), which determines the highest spatial frequency sampled, and the angular step size ($\Delta\theta$). (Brown, Cheng, et al. 2014, p.306)

The 'golden-angle' strategy, which was used in this work, optimizes this approach by spacing the radial lines at an angle of approximately 111.25 degrees. This specific angle helps in continuously covering the k-space without overlapping lines, ensuring that each new image frame provides unique information, thus enhancing image quality and temporal resolution.

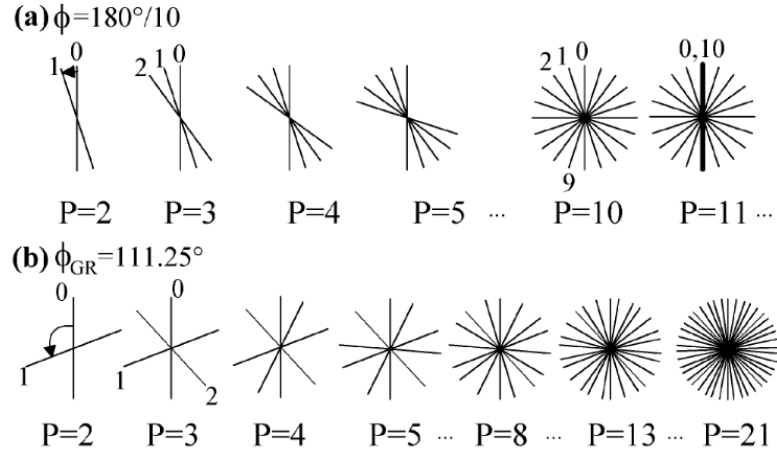


Figure 11: Radial k-space sampling strategies. (a) Fixed angular increment ($\phi = 180^\circ/10$), showing potential for uneven k-space coverage. (b) Golden-angle sampling ($\phi_{GR} = 111.25^\circ$), ensuring uniform distribution across k-space as the number of projections (P) increases (Winkelmann, Schaeffter, et al. 2007).

Figure 11 provides a visual comparison between traditional fixed increment and the golden-angle methods in k-space sampling. It highlights how each approach affects the distribution of sampling lines across k-space. In the figure, part (a) shows radial sampling using a fixed angular increment. This traditional method can lead to gaps or overlaps in data collection, depending on the number of radial profiles used. Part (b) demonstrates the golden-angle method, where each new radial line is placed at an increment of approximately 111.25 degrees. This approach allows for a more uniform distribution of sampling lines across k-space, enhancing image quality by preventing gaps and reducing redundancy in data collection. Figure 12 is an example of the k-space data acquired during a specific frame of the knee flexion cycle along with the reconstructed MRI image in real space obtained by applying an inverse 2D Fast Fourier Transform (2D IFFT) to the k-space data.

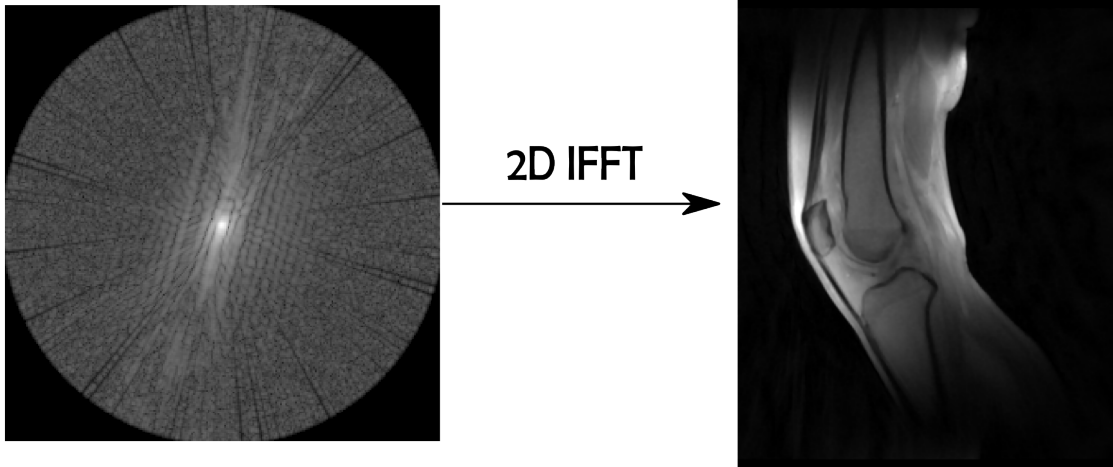


Figure 12: Left: Exemplary k-space data acquired during a specific frame of the knee flexion cycle. Right: Reconstructed MRI image in real space obtained by applying an inverse 2D Fast Fourier Transform (2D IFFT) to the k-space data

3 Methodology

3.1 Data Collection Methods

3.1.1 Procedure Details

Dynamic MRI scans were conducted on five healthy individuals, two females and three males, ranging in age from 28 to 39 years and weighing between 55 to 90 kilograms, utilizing a 3 T Siemens Prisma fit scanner. These volunteers were free from any known musculoskeletal disorders and provided their written consent, adhering to the ethical standards approved by the institutional review board. For all of these subjects, the left leg was scanned. In total, 7 unique datasets were acquired.

Once the subject was positioned supine in the scanner, the thigh was secured on a wedge positioner, and the lower leg was attached to an ankle rest, just above the malleoli, using Velcro straps to minimize lateral movement. The knee to be examined is aligned with the device's axis of rotation, while the other leg rests alongside the MRI scanner's bore. Knee motion is guided by a belt and sprocket assembly running alongside the lower leg, connected to a gearbox activated by the leg support as the participant flexes and extends the knee. Once the subject was positioned at the scanner's isocenter, their leg naturally assumed a flexed posture due to the design of the device. In this configuration, the leg is cradled by the device

arm which is positioned below the level of the knee, ensuring that the leg remains flexed without the volunteer exerting any force.

The volunteer engaged in a controlled exercise, following a metronome set at 60 beats per minute. This pace dictates a four-beat flexion to extension cycle, with the leg being flexed at the first beat and fully extended by the fourth. This equals to 8 beats per cycle, or 7.5 cycles every minute. Initially conducted under a loaded condition, the process is repeated without the added resistance to compare both states. The scan duration is 160 seconds, amounting to 20 full flexion-extension-flexion cycles. The range of motion for each dataset is noted in table ??.

Table 1: Range of Motion for Different Datasets

Dataset	Range of Motion (°)
1	30
2	38
3	36
4	30
5	36
6	36
7	46

3.1.2 Sequence Parameters and Reconstruction

Table ??, lists the MRI sequence parameters along with their respective units.

Table 2: MRI Sequence Parameters

Sequence Parameters	Values
Dimensions of raw data	(352, 276, 16, 100)
Acquisition Duration	160 [s]
Dwell Time	0.0024 [ms]
Echo Time	2.51 [ms]
Field Strength	2.89362 [T]
Flip Angle	8.0 [degrees]
Field of View (FOV)	192.0 x 192.0 x 3.0 [mm]
Frequency	123.25 [MHz]
Inversion Time	150000 [ms]
Matrix Size	176 x 176 x 1
Repetition Time	5.8 [ms]

In this study, the k-space data was acquired using 16 receive channels, each recording data simultaneously but with a unique spatial sensitivity profile. With 276 spokes used to sample a k-space dataset and a repetition time (TR) of 5.8 milliseconds per spoke, it takes approximately 1.6 seconds to acquire one k-space data. Over the course of the experiment, 100 such k-space datasets are acquired, equaling 100 repetitions as noted. The total scan duration extends just over two and a half minutes, a time frame reported by the subjects as being manageable, regardless of whether the scan was conducted under loaded or unloaded conditions.

Each k-space dataset contained data across a range of knee angles because of the continuous leg movement set to the metronome beat. This means, assuming the subjects perform perfectly in time of 60 beats per minute where we have 4 beats for flexion to extension, each k-space covers 0.4 times the range of motion. For example, a subject with a range of motion of 40° , each k-space dataset contains data across 16° . Therefore, with multiple repetitions, data across the full range of motion could be adequately acquired.

Reconstruction

The MRI raw data, with dimensions of (352, 276, 16, 100), was processed using a reconstruction script to generate the final image dataset. These dimensions correspond to:

- 352: The number of data points per spoke.

- 276: The number of spokes used to sample a k-space dataset.
- 16: The number of receive channels
- 100: The number of repetitions or k-space datasets acquired over the course of the experiment.

First, the binary data from the optical sensor was loaded, and the physical angle information was grouped according to each repetition cycle. This was done by detecting significant changes in the trigger signal, which was obtained from the sensor data too. This grouping resulted in 100 groups, each containing the physical angle information for a specific repetition. For each repetition, spokes in k-space were assigned to their corresponding physical angles. An angle increment of 2 degrees was chosen, which led to a collection of spokes corresponding to each 2-degree range. This approach was applied to all repetitions, allowing spokes to be mapped to physical angles across the full range of motion.

Subsequently, reconstruction was performed on each group of spokes. Depending on the specific angle range, the number of spokes assigned varied between 300 and 1000. Additionally, the direction of leg movement—either from flexion to extension or vice versa—was determined by calculating the slope of the angle information. Images were then reconstructed separately for each direction, depending on whether the leg was moving upward or downward. This distinction is crucial because leg biomechanics vary significantly depending on whether the movement is working with or against gravity.

The use of riesling toolbox

The actual image reconstruction was done by using the Riesling reconstruction toolbox (Wood and contributors 2020). This toolbox offers a range of advanced algorithms tailored for non-Cartesian MRI reconstruction. In this study, an Alternating Direction Method of Multipliers (ADMM) approach was employed, incorporating Total Generalized Variation (TGV) regularization.

ADMM is an iterative optimization algorithm that breaks down complex problems into smaller subproblems to solve them efficiently. It ensures accurate reconstruction by maintaining a balance between the primal (actual solution) and dual (approximate solution) residuals. This balance is particularly important for non-Cartesian MRI reconstruction, given the unique geometry of the data. ADMM allows different regularization techniques, like TGV, to be applied simultaneously during reconstruction (Boyd, Parikh, et al. 2011).

TGV is an advanced regularization method that reduces noise while promoting smoothness in the reconstructed images. Unlike basic Total Variation (TV) regularization, TGV allows for piecewise smooth transitions between different regions, making it better suited for images with varied structures. In this study, a regularization strength of 0.05 was chosen empirically, striking a balance between noise suppression and edge detection.

The final reconstructed images were affected by the chosen reconstruction parameters, including the zero-filling factor and the field of view (FoV) trimming factor. The use of TGV regularization and the ADMM algorithm influenced the resulting image resolution, providing images with a consistent size suitable for downstream analysis. Each image frame was reconstructed with dimensions of (528, 528) and the number of frames were subject dependent (range of motion).

3.2 Data Analysis

All the analysis and data visualization were done using the python programming language (v3.11.5). Several distinct steps were performed to semi-automate the segmentation of tibia and femur. This involves first finding one boundary edge each for the bones, and then tracking them across the full flexion-extension cycle by computing their respective transformation matrices.

3.2.1 Segmentation

The semi-auto segmentation process is achieved in five distinct steps as described below:

Step 1: Edge Detection

The Canny filter (Canny 1986), as implemented in the scikit-image's feature library (v0.21.0), was employed to apply an edge filter to the images. The Canny edge detection algorithm operates in several key steps to identify edges with high accuracy in images. Initially, the image is smoothed using a Gaussian filter to reduce noise and potential false edge detections. Following this, the algorithm calculates the gradient intensity and direction at each pixel, which helps in identifying the edges' boundaries.

Subsequently, the algorithm applies double thresholding, which involves two thresholds: a low and a high. This creates three categories of pixels: strong, weak, and

non-edges. Pixels with intensities above the high threshold are marked as strong edge pixels, while those below the low threshold are considered to be non-edges. Pixels between these two thresholds are marked as weak edge pixels. Weak edge pixels are potentially converted into strong edges through a process known as hysteresis, where only those weak edges that are connected to strong edges are confirmed as true edges. In this context, hysteresis refers to the algorithm's reliance on the connectivity history of pixels to decide their edge status, ensuring that only meaningful, connected edges are preserved. This step is crucial for ensuring the continuity and completeness of detected edges.

To optimize the edge detection specifically to capture the desired edges of the tibia and femur, the different parameters like the standard deviation of gaussian blur (sigma) and the thresholds were tested in different combinations. The optimal results were achieved with a low threshold between 0 to 5 and a high threshold between 6 to 10. The sigma value was set at 2. Figure 13 displays the output of with these parameters.

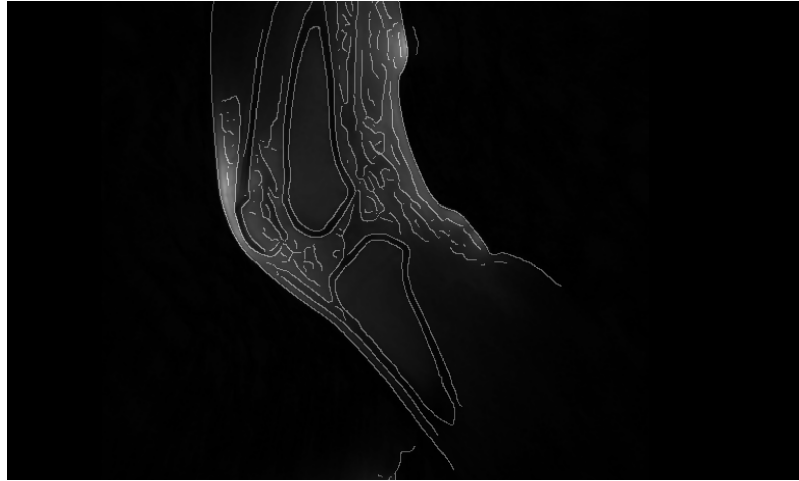


Figure 13: Output of the Canny edge detection algorithm applied to one of the frames, showing the detected edges of the tibia and femur bones overlayed on top of the original image for visual comparison.

Subsequently, the scikit-image's morphology library was utilized to remove small elements from the binary image. The image was then skeletonized to a one-pixel width, retaining only long and consistent edges. It should be pointed out that the final edge does not necessarily need to span the full boundary of the interior edge of the cortical bone; even partial edges were successfully used for this purpose.

Step 2: Labelling

For the final selection of the desired edges, a labeling algorithm ('ndimage.label') from SciPy, an open-source Python library designed for scientific computing (version 1.11.3), was utilized. The purpose of employing this labeling algorithm is to effectively isolate specific structural features, such as distinguishing the interior cortical bone from the exterior, by assigning unique labels to separate closely situated edges detected in the image. This algorithm applies the principle of connected-component labeling, a method used in computer vision to detect connected regions in binary digital images. Connected-component labeling algorithm scans an image and groups its pixels into components based on pixel connectivity, meaning that all pixels in a connected component share similar pixel values and are adjacent to each other.

The labeling process treats any non-zero values in the input array as part of potential edges and zero values as background. The connectivity of these components is determined by a structuring element, which in this case was a fully connected 3x3 matrix:

$$\begin{bmatrix} 1 & 1 & 1 \\ 1 & 1 & 1 \\ 1 & 1 & 1 \end{bmatrix}$$

This matrix is crucial as it defines the connectivity rules used during the labeling. Each pixel is considered connected to its eight immediate neighbors (above, below, left, right, and diagonals), known as eight-way connectivity. This element was chosen by trial and error. Alternatives, such as a four-way connectivity matrix, were tested but gave different labels to the same edge across frames. By using the eight-way connectivity, the same edge maintains consistent labeling across all frames, simplifying the analysis and reducing the need for manual adjustments.

Figure 14 shows the output from the labelling algorithm, where each color represents a separate label.

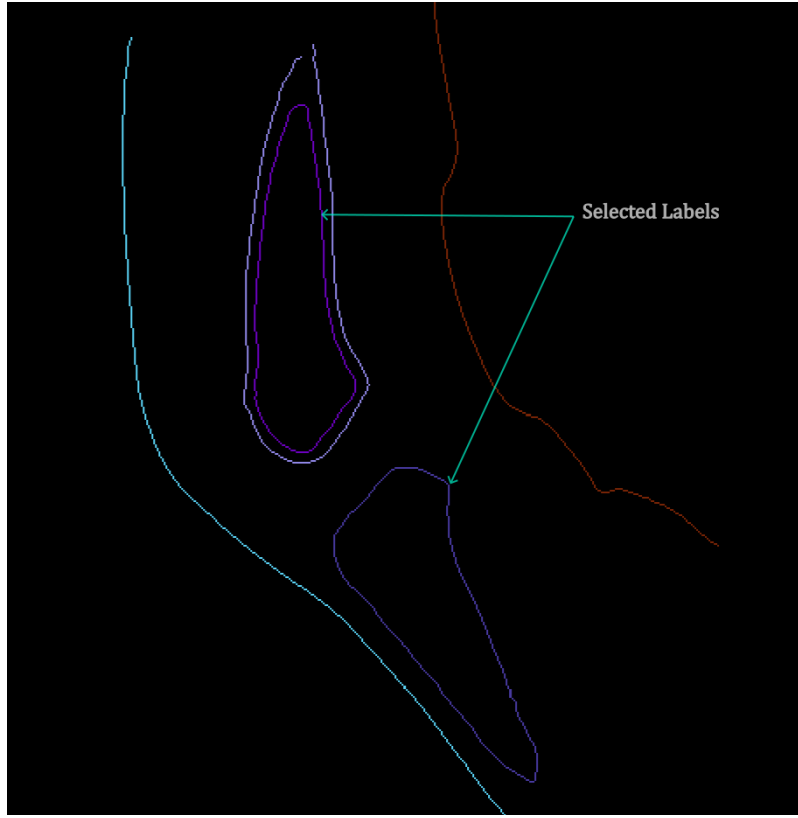


Figure 14: Output from the labeling algorithm with the representative edges for femur (top) and tibia (bottom) highlighted. Distinct colors represent a different label identified by the labeling algorithm.

After choosing the appropriate labels, a binary image for each frame is obtained, where the foreground has the boundary for the interior edge of tibia and femur, and the background has intensity value of zero.

Step 3: Obtaining the set of reference points

Upon successfully isolating the binary edge images of the tibia and femur in Step 2, the subsequent step deals with establishing a set of reference points along each bone's edge in the first frame. This frame, captured when the knee is in a fully flexed position, serves as the reference frame for further analysis. This frame is chosen as the baseline (where transformations are initialized to zero) to facilitate the accurate calculation of rotation and translation matrices that describe the movement of the knee through subsequent frames. The purpose of establishing these reference points is twofold: to simplify the complex data set for efficient processing and to ensure a consistent basis for accurately calculating transformations between subsequent frames. This is essential, as direct use of the densely packed binary edge data would be computationally cumbersome and less precise for such transformations.

To begin, the points along the boundary were organised and sorted. This was done by first, defining a starting point, and then iteratively using a greedy nearest neighbor algorithm for sorting. The most distal point of the bone was taken as the initial seed. Various functions from the numeric python library 'Numpy' (v. 1.26.4) were employed for this task.

Once the points are sorted, the next step involves downsampling these points to a set of uniform equidistant reference points along the boundary of the binary edge. The necessity for this step arises from the inherent irregularity and density of the binary edge data. Directly sampling every n-th point from the sorted list would not suffice, as it could result in uneven spacing due to the variable distances between consecutive points in the original data.

This process begins by calculating the cumulative distances between each consecutive pair of points in the sorted list. Using these distances, a total path length is established. The desired interval between the new points is then determined by dividing this total path length by the number of intervals (number of desired points minus one).

Determining the optimal number of points—ranging between 50 to 80—was established through trial and error. Fewer than 50 points often compromised the accuracy of the edge overlap by failing to capture the essential contours of the bone. Conversely, exceeding 80 points did not significantly enhance the algorithm's accuracy but increased the code execution time slightly.

To achieve precise positioning of these points, cubic spline interpolation from SciPy's interpolate library was used. This interpolation method is particularly effective for ensuring that the new points adhere closely to the original curve while maintaining equidistance. Figure 15 depicts this result.

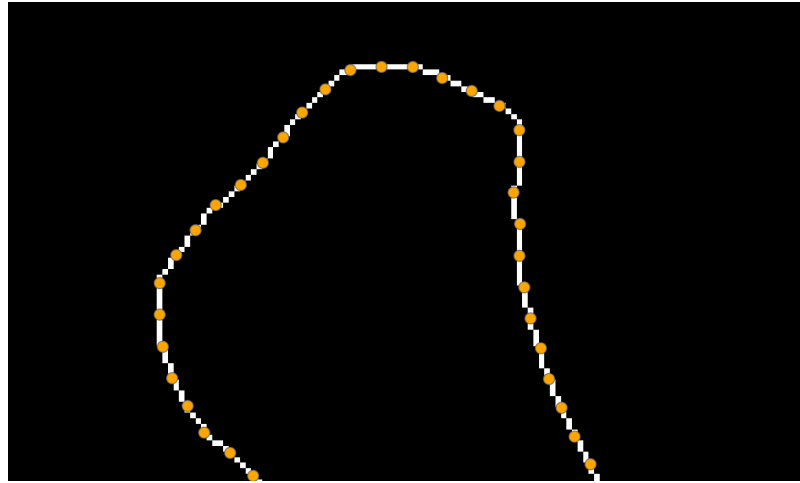


Figure 15: A zoomed in look at the equidistant sampled points (orange) along the boundary of the tibia edge (white).

Step 4: Transformation matrices computation

In this step, a set of transformation matrices is obtained, each containing the parameters that align a segment of the bone from one frame to the next. These transformations includes solely the translation in the sagittal plane and rotation about the transverse axis. This approach assumes that the bone does not undergo any deformation and that through-plane motion is negligible throughout the motion cycle.

Mathematically, the transformation of each point from one frame to the next can be expressed as

$$p' = R(\phi)p + t \quad (2)$$

where:

- p is the coordinate of the point in its current frame
- p' is the coordinate of the point after transformation
- ϕ is the angle of rotation
- $R(\phi)$ is the rotation matrix, given by

$$R(\phi) = \begin{bmatrix} \cos \phi & -\sin \phi \\ \sin \phi & \cos \phi \end{bmatrix}$$

- t is the translation vector,

$$t = \begin{bmatrix} x \\ y \end{bmatrix}$$

- x and y are the translations in the Cartesian coordinate system.

As such, only three parameters, x , y , and ϕ need to be computed. To determine these parameters, a cost function is defined. This function, denoted as $C(x, y, \phi)$, quantifies the alignment error by calculating the 'cost' of deviations for any given set of transformation parameters. The minimization of this cost identifies the combination of parameters that achieves the best alignment or overlap of the transformed frame with the reference frame. A lower value of the cost function output indicates a closer match to the target frame, suggesting a superior alignment, whereas a higher value signifies a less accurate alignment. The cost function is defined in Equation 3:

$$C(x, y, \phi) = \sum_{p=1}^N \min_{q \in Q} \left(\sqrt{(x_q - x'_p)^2 + (y_q - y'_p)^2} \right) \quad (3)$$

where:

- (x_p, y_p) are the coordinates of points in the reference frame
- (x'_p, y'_p) are the coordinates of points after transformation:

$$\begin{aligned} x'_p &= x + x_p \cos(\phi) - y_p \sin(\phi) \\ y'_p &= y + x_p \sin(\phi) + y_p \cos(\phi) \end{aligned}$$

- (x_q, y_q) are the coordinates of points in the target frame.
- N is the number of points in the reference frame, and Q represents all points in the target frame.

This cost function evaluates the alignment of transformed coordinates to target coordinates by calculating the sum of the shortest distances from each point in the transformed frame to the closest point in the target frame. Each (x'_p, y'_p) is the position of a point from the reference frame after being transformed by the parameters x , y , and ϕ . For each transformed point, the distance to every point (x_q, y_q) in the target frame is computed, the minimum of these distances is selected,

and sum these minimum distances across all points is calculated. This sum forms the output of the cost function, which we seek to minimize.

The optimization of this cost function is performed using a nonlinear least squares approach, where the initial guess of $[0,0,0]$ is provided. This guess represents the starting point for the transformation parameters x , y and ϕ . The `fmin` function from SciPy's optimization module is used for this purpose, which uses the Nelder-Mead simplex method (Nelder and Mead 1965). The function is configured with a function tolerance and parameter tolerance of 1×10^{-8} , and maximum iterations of 1000. This method iteratively explores the parameter space to find the set of parameters that result in the lowest cost function value. The optimization procedure continues until the change in the cost function is less than the specified tolerance or the maximum number of iterations is reached, indicating convergence to an optimal solution. Figure 16 provides a visual representation of the overlap of the reference points from the fully flexed initial position to the frame where the lower leg has been rotated by an angle of 12 degrees as reported by the rotary angle encoder.

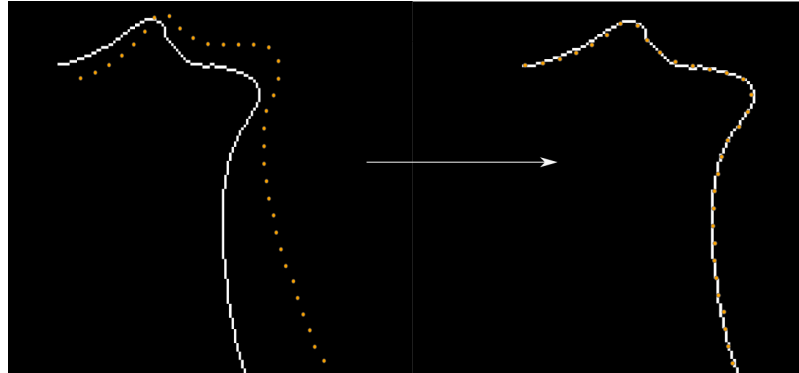


Figure 16: Left: The reference points in the first frame (orange) overlaid with the binary edge image of the target frame (white). Right: The reference points have been transformed by using the results from the optimization showing almost perfect overlap, illustrating the effective alignment achieved through the minimization of the cost function.

Step 5: Auto-Segmentation

With the transformation matrices obtained for the femur and the tibia, manual segmentation is performed on the first frame. An example is given in figure 17.

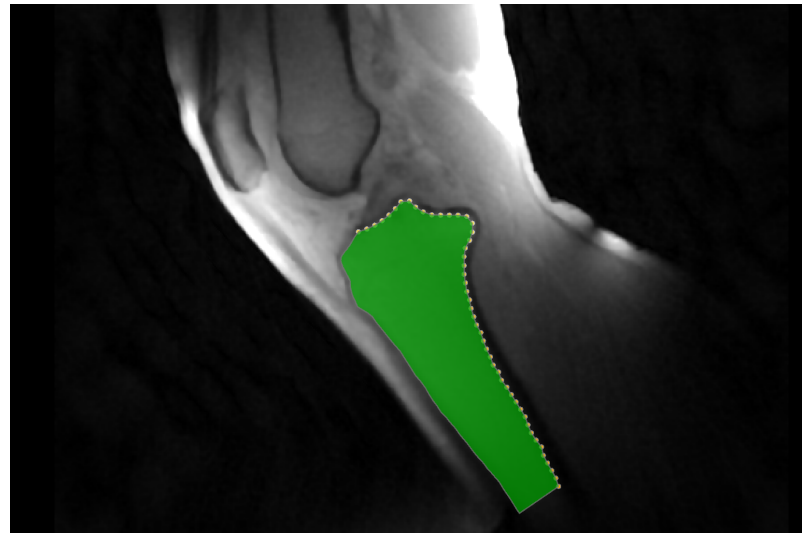


Figure 17: Manual segmentation is performed to complete the boundary of the tibia's interior edge shown in green, along with the reference points (orange).

Using the points from this segment, the transformation matrices are now applied once more using equation 2 to transform one frame to the next subsequently to complete the full segmentation across all the frames automatically.

3.2.2 Extraction of Biomechanical Parameters

After achieving automated segmentation of the tibia and femur across all frames, the next step involved extracting biomechanical parameters from the segmented regions. Two key metrics were considered for analysis to assess the relationship between these bones throughout the flexion-extension cycle captured in the 2D Cine images.

The first metric involved calculating the angle between the long axis of femur and tibia segments. This measurement provided insight into how the relative orientation of the two bones changes over time.

The second metric measured the distance between specific anatomical landmarks on both the femur and tibia. Tracking this distance across the frames offered an understanding of how the spatial relationship between these two bones evolved during the motion cycle.

Angle between the bones

To calculate the angle between the bones, the long axis of each bone segment was identified using a technique called Principal Component Analysis (PCA). The anal-

ysis was performed using the PCA implementation from the scikit-learn (v1.3.1) Python library, a module for machine learning built on top of SciPy.

PCA determines the direction of maximum variance in the data, which coincides with the longitudinal axis of the bone. PCA first uses the coordinates of the segmented binary mask as input. The centroid of the shape is calculated and subtracted from each data point, centering the data such that the mean of this transformed data is $(0, 0)$.

Next, the covariance matrix (Cov) is computed, a square matrix that gives an indication of how the data varies along each dimension and how different dimensions vary together.

$$\text{Cov} = \begin{bmatrix} \text{Var}(X) & \text{Cov}(X, Y) \\ \text{Cov}(Y, X) & \text{Var}(Y) \end{bmatrix} \quad (4)$$

where:

- $\text{Var}(X)$ is the variance of X , given by:

$$\text{Var}(X) = \frac{1}{N-1} \sum_{k=1}^N (X_k - \bar{X})^2,$$

where N is the number of points, X_k represents the k^{th} observation in the X dimension, and \bar{X} is the mean value of all observations in the X dimension.

- $\text{Cov}(X, Y)$ is the covariance between dimensions X and Y , defined as:

$$\text{Cov}(X, Y) = \frac{1}{N-1} \sum_{k=1}^N (X_k - \bar{X})(Y_k - \bar{Y}),$$

where Y_k represents the k^{th} observation in the Y dimension, and \bar{Y} is the mean value of all observations in the Y dimension.

- $\text{Cov}(Y, X)$ is equivalent to $\text{Cov}(X, Y)$ because the covariance matrix is symmetric.
- $\text{Var}(Y)$ is the variance of Y , calculated similarly to $\text{Var}(X)$.

When this covariance matrix is applied to a vector, the matrix transforms the vector such that it aligns more closely with the direction of maximum variance in the

dataset. Therefore, by computing the matrix's eigenvectors and eigenvalues, the vectors representing the direction of maximum variance is identified. The first principal component refers to the eigenvector associated with the largest eigenvalue. In figure 18, the longitudinal axis of femur and tibia are shown.

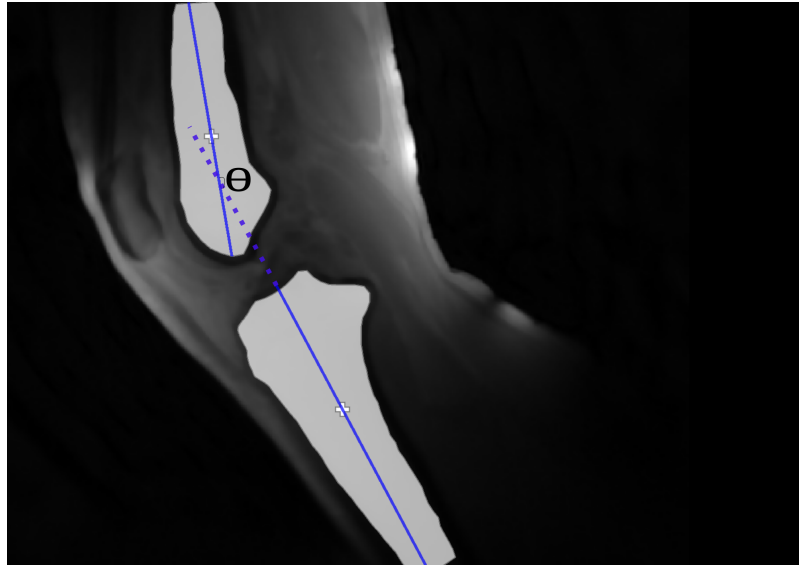


Figure 18: The long axis of the bones are identified by using the PCA (blue) along with the centroid (white cross) for each segment. θ represents the angle that is being measured

The angles between the segments was calculated by using the dot product between unit vectors, as given in equation 5

$$\theta = \arccos(\mathbf{U}_{fem} \cdot \mathbf{U}_{tib}) \quad (5)$$

where, \mathbf{U}_{fem} and \mathbf{U}_{tib} are the unit vectors of the longitudinal axes for the femur and tibia segments respectively. For visualization purposes, when the knee is hyperextended, angles greater than 180° are reported to clearly indicate the degree of hyperextension. Therefore, in graphs presenting the results, the peak angle can exceed 180° (e.g., 185°) to represent hyperextension.

Distance between the bones

To calculate a proxy for the distance between the bones, anatomical landmarks were identified for the bones. The most distal point on the femur segment was chosen for the femur and a point on the proximal tibia for the tibia as shown in figure 19.

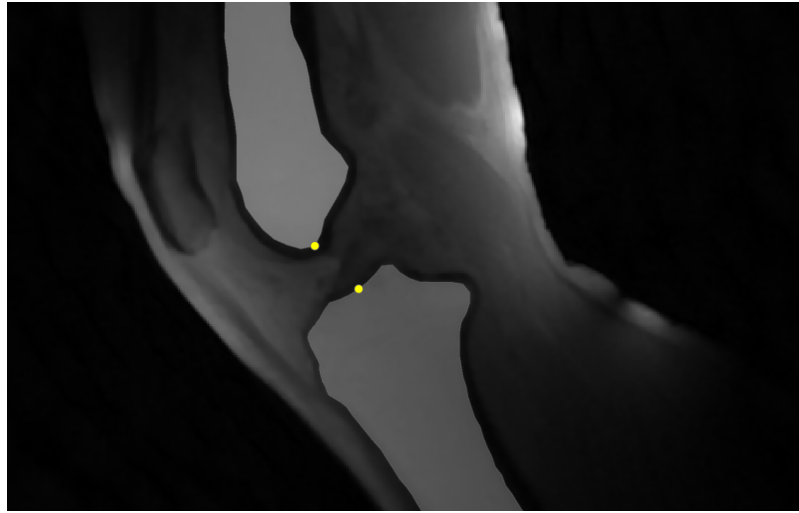


Figure 19: Points based on anatomical landmarks are shown in yellow.

The euclidean distance between these two points was measured across time by using equation 6. The first frame at -100% flexion is considered as the baseline, with the distance set to 0 mm. All subsequent distances are relative to this baseline, enabling an analysis of changes across the cycle.

$$d = \sqrt{(y_2 - y_1)^2 + (x_2 - x_1)^2} \quad (6)$$

Negative values imply the distance has decreased with respect to the baseline (first frame).

4 Results

4.1 Edge tracking and segmentation

To evaluate the accuracy of edge tracking achieved through cost function minimization, the deviation of overlap between points on the transformed frame and the target frame was measured. The cost function output, which indicates the overlap accuracy, calculates the minimum distance from each point on the transformed frame to the points on the target frame and sums these minimum distances for all points in the transformed frame.

The mean alignment error per point was then derived by dividing the cost function output by the total number of points in the transformed frame. This value quantifies the average distance that a point on the transformed frame deviates from its

corresponding point on the target frame. This value was calculated for all frames, and the average of these values was taken for each dataset.

The bar chart in Figure 20 presents this result:

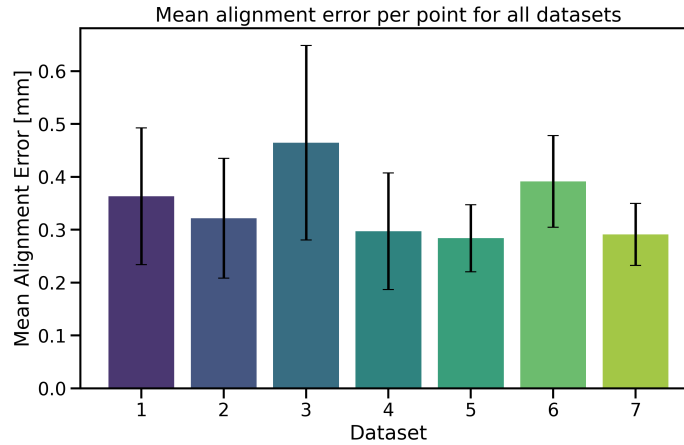


Figure 20: Mean alignment error per point across all frames for each tibia dataset.

The result of the segmentation for one of the datasets is given in figure 21.

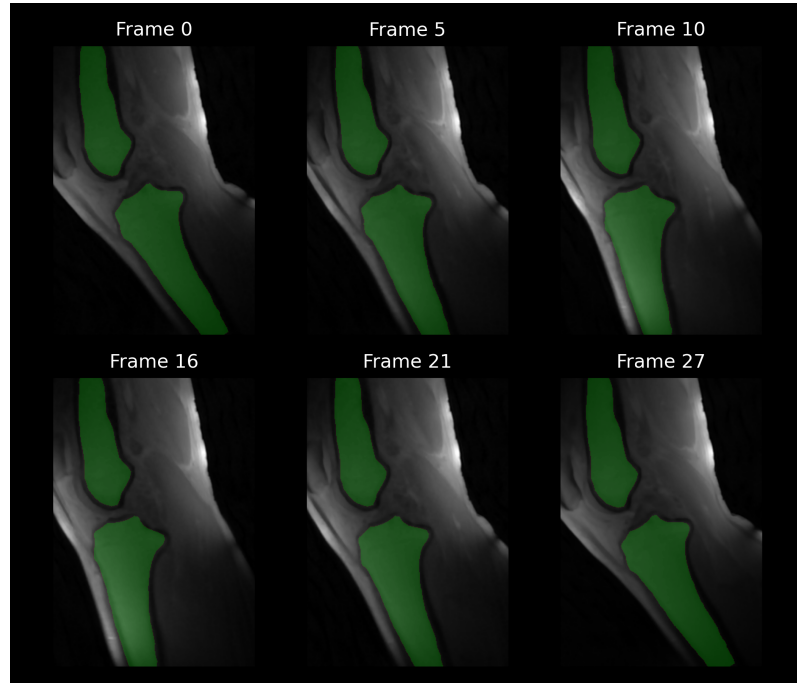


Figure 21: A mosaic showing the segmented tibia and femur shapes(green) where each tile is a particular time point. The leg is fully flexed at Frame 0

4.2 Biomechanical parameter extraction

The changes in the angle between the long axes of the tibia and femur segments, as well as the distance between these segments, were measured throughout the flexion-extension cycle for both the loaded and unloaded conditions.

To enable consistent comparisons across different datasets, the number of frames from each motion cycle was normalized by grouping the data into 'bins'. This binning process ensured that all datasets spanned the same range, allowing for the averaging and plotting of values within these bins.

The x-axis of the graphs represents the percentage of the flexion-extension cycle, defined by the bin centers. The cycle starts at -100 % (maximal flexion), progresses to 0 % (full extension), and returns to 100 % (maximal flexion). This labeling captures the complete motion cycle, from full flexion to full extension and back to full flexion, allowing a clear visualization of the entire range of motion. The x-axis ticks correspond to the centers of these bins, with each bin having a width of 10 percentage units.

The y-axis of the graphs represents the average value of the biomechanical parameter (either angle or distance) within each bin, aggregated across all datasets.

For statistical analysis, a two-sample independent t-test was performed using the `stats` module from the SciPy library to compare the loaded and unloaded conditions. The test was applied to the data within each bin to determine if there were significant differences between the two conditions.

Angle calculation

Figure 22 displays the result of calculating the angle between the long axes of bone segments across the flexion-extension cycle.

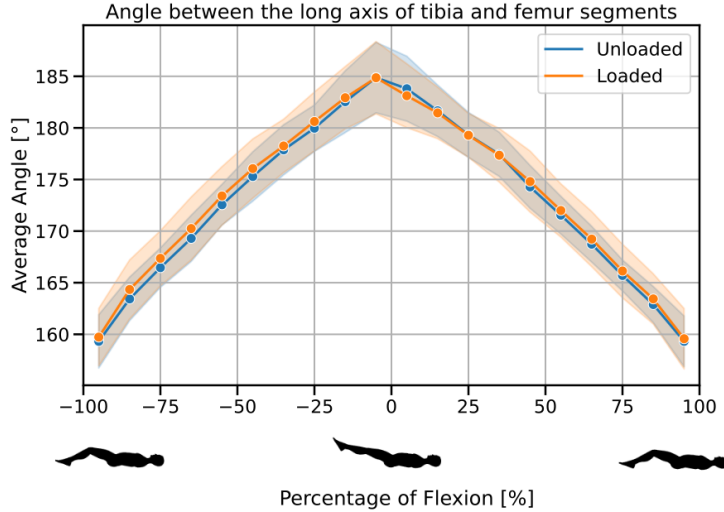


Figure 22: Plot of angle between long axes of bone segments between tibia and femur versus the flexion percentage. The x-axis ticks represent the centers of bins, each with a width of 10 percentage units. The shaded regions represent one standard deviation uncertainty. Angles greater than 180° imply hyperextension.

No significant differences were observed between the loaded and unloaded conditions for any of the bins.

Distance calculation

The Euclidean distance between two points on the tibia and femur segments was measured throughout the flexion-extension cycle for both loaded and unloaded conditions. The aggregated results are shown in Figure 23

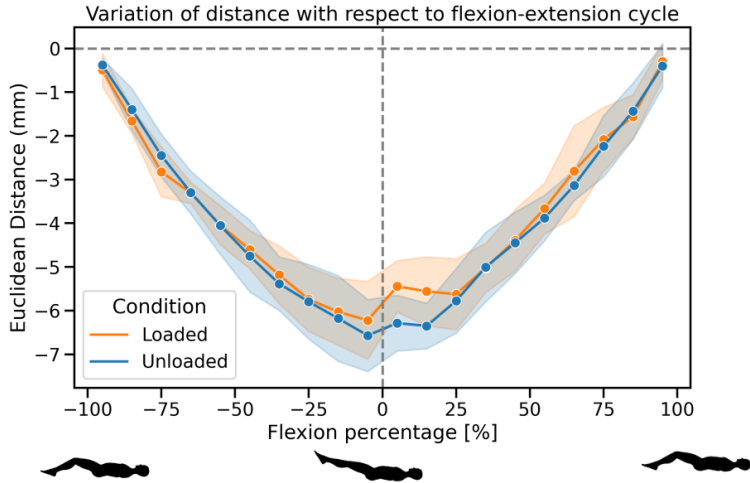


Figure 23: Plot showing the variation of euclidean distance between two points with across time in the motion cycle. All distances are relative to the baseline measurement at -100% flexion, set at 0 mm. The shaded region represents one standard deviation uncertainty.

Statistical analysis revealed significant differences between loaded and unloaded conditions in the following bins: (0.0, 10.0] with a P-value of 0.022, and (10.0, 20.0] with a P-value of 0.015. No significant differences were observed for the remaining bins.

5 Discussion

The accuracy and reliability of the measurements obtained from the dynamic MRI scans are influenced by several factors that need to be considered to ensure meaningful results. One significant factor is the overall bulk movement of the leg during the scan. If the femur is not properly fixated, the entire leg might shift, leading to inaccurate measurements. Ensuring that the thigh is securely positioned on the device with the thigh strap is critical for minimizing this movement. Additionally, improper fixation can allow the upper leg to lift or shift laterally, further compromising the accuracy of the measurements. This overall instability can be exacerbated by the entire leg shifting longitudinally within the scanner, causing misalignment and poor-quality output.

Another important factor is muscle exhaustion. At the start of the exercise, volunteers might overexert themselves, leading to fatigue as the exercise progresses.

This can cause variations in the range of motion and affect the position of the leg, resulting in inconsistent data. While the controlled exercise pace, guided by a metronome, aims to standardize the movement, individual differences in endurance can still introduce variability.

By addressing these factors, we can enhance the reliability of the measurements obtained from the dynamic MRI scans. With these considerations in mind, the following sections discuss the specific results of edge tracking and segmentation, angle measurement, and distance calculation in detail.

5.1 Edge tracking and segmentation

The accuracy of segmentation in this study is fundamentally tied to the precision of edge tracking, as the segment boundary is defined by the detected edges. A significant factor that compromises edge tracking accuracy is the through-plane motion of the bones, leading to inaccurate transformations. The algorithm is specifically designed to manage only rigid transformations within a single plane; therefore, any deviations introduced by through-plane motion significantly impair edge detection and, consequently, segmentation accuracy.

Through-plane motion is particularly problematic for the tibia compared to the femur, primarily due to medial/lateral rotation as illustrated in Figure 4, which details the six degrees of freedom of the tibia’s movement relative to the femur. This specific type of rotation is a significant cause of through-plane motion errors during edge tracking, as the device setup—although restrictive—allows some degree of rotational freedom. Despite the lower leg being secured at the ankle with Velcro straps and the knee cradled in a wedge positioner to limit movement predominantly to one plane, complete immobilization is not achievable. This limitation is especially pronounced in subjects with smaller bones, where even additional padding at the wedge positioner was insufficient to prevent all undesired motion. While localizers are employed prior to the scans in both extended and flexed positions to ensure that the slice moves only within a predetermined single plane, certain rotations cannot be fully corrected by simply angling the localizer and may still be evident in the final images.

The performance of the edge tracking algorithm is illustrated by the bar chart in Figure 20, which shows the mean alignment error per point across seven different datasets in millimeters. Datasets 2,4,5 and 7 show the lowest mean alignment error

around 0.3 mm, with Dataset 5 having the lowest error of 0.283 mm and standard deviation of 0.063 mm. In contrast, Dataset 3 exhibits the highest mean alignment error at about 0.465 mm and also shows the largest variability with a standard deviation of 0.184 mm. This variability and higher error could suggest specific challenges in edge detection for this dataset, potentially due to factors such as through-plane motion or variations in image quality. The low standard deviation for 7, at 0.059 mm with a mean alignment error of 0.291 mm, further suggest that the edge tracking performance in this dataset was not only accurate but also consistently reliable across different frames.

To illustrate the reliability of the edge tracking algorithm, the results obtained here are compared with those of Rathnayaka et al.(2012), who quantified the accuracy of MRI-generated 3D models of long bones, reporting an average error of 0.23 mm (Rathnayaka, Momot, et al. 2012). Although the specifics of the two studies differ, the reported values offer a perspective on the range of errors encountered in MRI-based segmentation measurements.

5.2 Angle calculation

The analysis of the angle between the long axes of the tibia and femur segments across the flexion-extension cycle reveals distinct trends under both loaded and unloaded conditions. As illustrated in Figure 22, there is a clear pattern where the angle increases from approximately 160° at maximal flexion (-100%) to around 184° at full extension (0%), and then decreases back to 160° as the knee returns to maximal flexion (100%). This behavior aligns with the expected biomechanics of the knee joint, where the alignment of the femur and tibia is closest at full extension and diverges during flexion.

To provide specific data points, at a bin center of -5 (representing the range from -10 to 0, inclusive), the mean angle for the unloaded condition was 184.18° with a standard deviation of 4.04°, while for the loaded condition, the mean angle was 184.07° with a standard deviation of 3.99°. These measurements indicate that both conditions exhibit angles close to 185°, suggesting a slight hyperextension or at least a deviation from a perfectly straight alignment.

This observed deviation can be explained by the nature of the angle measurements and the biomechanics of the knee joint. The angles calculated in this study are best represented by the shaft axes of the femur and tibia. As demonstrated by a

study (Dai, Sha, et al. 2021) which measured the knee flexion angle using CT and MRI, a range of values was reported between -12.5° and 29.9° , where negative values indicate hyperextension. Since these values are obtained from static scans, where the leg is in an extended position inside the scanner, it can be assumed that at full extension, angles greater than 180° as measured in this study are to be expected. Their scheme for defining the angles closely match to those done in this study, as given in Figure 24.



Figure 24: Femur (a) and tibia (b) shaft axes defined in CT and T1-weighted MRI scans in the sagittal view. (Dai, Sha, et al. 2021)

Interestingly, despite the observed angles suggesting a slight hyperextension, there was no significant difference in the angles between the loaded and unloaded conditions. This indicates that the loading condition did not significantly affect the alignment of the femur and tibia as measured by the angle between their long axes in the sagittal plane.

5.3 Distance calculation

Figure 23 shows the variation in the Euclidean distance between anatomical landmarks on the femur and tibia throughout the flexion-extension cycle. Initially, this distance decreases as the knee moves from a flexed to an extended position. In the second half of the cycle, the distance increases as the knee returns to the flexed position.

Significant differences were observed in the bins $(0.0, 10.0]$ and $(10.0, 20.0]$ with P-values of 0.022 and 0.015 under loaded conditions. This suggests that external loading affects the spatial relationship between the femur and tibia, but only during the beginning of the flexion phase.

This suggests that there is an underlying mechanism influencing the measured distance near terminal extension but not during other phases of motion. A likely candidate for this is the screw home mechanism (SHM). The SHM involves the rotation of the tibia around the femur near terminal extension. It occurs due to the unequal lengths of the condyles. The medial femoral condyle is longer than the length of the lateral condyle, which causes the tibia to rotate externally in the last stages of extension. (Kim, Kim, et al. 2015) This rotation occurs to lock the knee in a stable, fully extended position. Then, when flexion starts during the second half of the cycle, the tibia rotates internally, which 'unlocks' the knee for further flexion.

It has been previously reported that the impact of external loading increases the magnitude of internal rotation of the tibia relative to the femur (Myers, Torry, et al. 2012). Therefore, it seems that this internal rotation is more susceptible to changes in the distance between the defined anatomical landmarks due to external loading compared to external rotation. This susceptibility likely results in the significant differences observed during the initial phase of flexion, as the knee transitions from a fully extended, locked position to a flexed, unlocked state.

Given these observations, it can be hypothesized that the response to external loading might serve as an indicator of SHM functionality. Notably, it has been demonstrated that SHM loss, characterized by reduced internal tibial rotation, occurs in patients with OA when compared to healthy controls, even without any applied external load (Jeon, Lee, et al. 2020). Additionally, quadriceps weakness has been identified as a significant risk factor for the development of OA (Segal and Glass 2011). This suggests that the external loading in our experimental setup, which induces quadriceps activation, could provide valuable diagnostic insights. Understanding the interaction between quadriceps strength and mechanical loading is crucial for detecting early signs of OA and developing targeted therapeutic strategies.

6 Conclusion

This study set out to explore the precision and practicality of a semi-automated segmentation process for analyzing dynamic MRI scans of the knee during flexion-

extension cycles. The findings demonstrate the potential of this method to accurately track and quantify biomechanical parameters such as bone alignment and distances between anatomical landmarks under different loading conditions.

Key Findings and Implications

The accuracy of the edge tracking and segmentation process was evaluated using the mean alignment error per point, which quantifies the average distance that a point on the transformed frame deviates from its corresponding point on the target frame. This metric was compared with similar values reported in the literature, revealing that our method provides a comparable level of precision in MRI-based segmentation measurements. Additionally, simple visual inspection also gives credence to the accuracy of the segmentation, further validating the reliability of the process. This semi-automated approach facilitates rapid and efficient analysis of large number of frames, making it highly advantageous for clinical and research applications. Moreover, once the bones are segmented, a wide range of biomechanical analyses can be conducted, providing comprehensive insights into joint mechanics, beyond those that were attempted in this study.

The analysis of the angle between the long axes of the tibia and femur showed no significant differences between loaded and unloaded conditions. Any deviation from this trend while measuring new subjects could indicate potential pathological issues.

The distance measurement between anatomical landmarks on the tibia and femur revealed significant differences between loaded and unloaded condition during the early phase of the flexion. This variation can be attributed to the screw-home mechanism, emphasizing the sensitivity of the knee joint's biomechanics to external loading. These findings underscore the importance of considering external loading in biomechanical analyses and suggest that the method could be a valuable tool for potential diagnosis and research.

Limitations and Future Work

Despite its promising results, this study's methodology is limited by its reliance on a single 2D slice. This approach overlooks the tibia's six degrees of freedom relative to the femur, potentially omitting critical aspects of knee kinematics. Future work should aim to extend this methodology to 3D, which would not only address current method's issues in edge tracking, but also allow for a complete assessment of knee joint kinematics, providing a more holistic understanding of its movements and interactions.

Additionally, the semi-automated segmentation method demonstrated here can be adapted to analyze patellofemoral kinematics. The patella shows well-defined edges in the images, making it a suitable candidate for this processing pipeline. Given the patella's significant role in knee mechanics, this extension would provide valuable insights and complement the current analysis of tibiofemoral interactions.

In conclusion, the semi-automated segmentation process evaluated in this study offers a robust and efficient method for analyzing dynamic MRI scans of the knee. By enabling accurate tracking of biomechanical parameters and accommodating various analyses, it presents a valuable tool for both clinical diagnostics and biomechanical research. While current limitations highlight the need for 3D analysis to fully capture knee kinematics, the potential applications of this method are vast, paving the way for more comprehensive and insightful studies of knee joint mechanics.

References

- Aleksiev, Martin et al. (Oct. 2022). "High-resolution CINE imaging of active guided knee motion using continuously acquired golden-angle radial MRI and rotary sensor information". In: *Magnetic Resonance Imaging* 92, pp. 161–168. ISSN: 0730725X. DOI: [10.1016/j.mri.2022.06.015](https://doi.org/10.1016/j.mri.2022.06.015).
- Bennell, Kim L et al. (June 2010). "Bone marrow lesions are related to dynamic knee loading in medial knee osteoarthritis". In: *Annals of the Rheumatic Diseases* 69.6, pp. 1151–1154. ISSN: 0003-4967, 1468-2060. DOI: [10.1136/ard.2009.118182](https://doi.org/10.1136/ard.2009.118182).
- Blankevoort, L., R. Huiskes, and A. De Lange (Jan. 1988). "The envelope of passive knee joint motion". In: *Journal of Biomechanics* 21.9, pp. 705–720. ISSN: 00219290. DOI: [10.1016/0021-9290\(88\)90280-1](https://doi.org/10.1016/0021-9290(88)90280-1). URL: <https://linkinghub.elsevier.com/retrieve/pii/0021929088902801> (visited on 05/20/2024).
- Boyd, Stephen et al. (2011). "Distributed Optimization and Statistical Learning via the Alternating Direction Method of Multipliers". In: *Foundations and Trends® in Machine Learning* 3.1, pp. 1–122. ISSN: 1935-8237. DOI: [10.1561/2200000016](https://doi.org/10.1561/2200000016). URL: <http://dx.doi.org/10.1561/2200000016>.
- Breivik, Harald et al. (May 2006). "Survey of chronic pain in Europe: Prevalence, impact on daily life, and treatment". In: *European Journal of Pain* 10.4, pp. 287–287. ISSN: 1090-3801, 1532-2149. DOI: [10.1016/j.ejpain.2005.06.009](https://doi.org/10.1016/j.ejpain.2005.06.009). URL: <https://onlinelibrary.wiley.com/doi/10.1016/j.ejpain.2005.06.009> (visited on 03/27/2024).
- Brisson, Nicholas M., Martin Krämer, et al. (Nov. 2022). "A novel multipurpose device for guided knee motion and loading during dynamic magnetic resonance imaging". en. In: *Zeitschrift für Medizinische Physik* 32.4, pp. 500–513. ISSN: 09393889. DOI: [10.1016/j.zemedi.2021.12.002](https://doi.org/10.1016/j.zemedi.2021.12.002). URL: <https://linkinghub.elsevier.com/retrieve/pii/S093938892100115X> (visited on 02/12/2024).
- Brisson, Nicholas M., João F. Oliveira, et al. (Apr. 2024). "Repeatability of knee joint motion during different load/speed protocols performed using a specialized device for dynamic magnetic resonance imaging". In: *Osteoarthritis and Cartilage* 32, S354–S355. ISSN: 10634584. DOI: [10.1016/j.joca.2024.02.519](https://doi.org/10.1016/j.joca.2024.02.519).
- Brown, Robert W. et al. (2014). *Magnetic resonance imaging: physical principles and sequence design*. Second edition. Hoboken, New Jersey: John Wiley & Sons, Inc. 944 pp. ISBN: 978-0-471-72085-0.
- Canny, John (Nov. 1986). "A Computational Approach to Edge Detection". In: *IEEE Transactions on Pattern Analysis and Machine Intelligence* PAMI-8.6, pp. 679–

698. ISSN: 0162-8828. DOI: [10.1109/TPAMI.1986.4767851](https://doi.org/10.1109/TPAMI.1986.4767851). URL: <https://ieeexplore.ieee.org/document/4767851> (visited on 02/18/2024).
- Coburn, Sally L. et al. (July 14, 2023). “Immediate and Delayed Effects of Joint Loading Activities on Knee and Hip Cartilage: A Systematic Review and Meta-analysis”. In: *Sports Medicine - Open* 9.1, p. 56. ISSN: 2198-9761. DOI: [10.1186/s40798-023-00602-7](https://doi.org/10.1186/s40798-023-00602-7). URL: [https://sportsmedicine-open.springeropen.com/articles/10.1186/s40798-023-00602-7](https://doi.org/10.1186/s40798-023-00602-7) (visited on 04/07/2024).
- Conconi, Michele et al. (Jan. 3, 2023). “In-Vivo Quantification of Knee Deep-Flexion in Physiological Loading Condition trough Dynamic MRI”. In: *Applied Sciences* 13.1, p. 629. ISSN: 2076-3417. DOI: [10.3390/app13010629](https://doi.org/10.3390/app13010629). URL: <https://www.mdpi.com/2076-3417/13/1/629> (visited on 05/20/2024).
- Curtis, Aaron D. and Hai-Ling M. Cheng (Feb. 2022). “Primer and Historical Review on Rapid Cardiac CINE MRI”. en. In: *Journal of Magnetic Resonance Imaging* 55.2, pp. 373–388. ISSN: 1053-1807, 1522-2586. DOI: [10.1002/jmri.27436](https://doi.org/10.1002/jmri.27436). URL: [https://onlinelibrary.wiley.com/doi/10.1002/jmri.27436](https://doi.org/10.1002/jmri.27436) (visited on 04/09/2024).
- d’Entremont, Agnes G. et al. (June 2013). “Do dynamic-based MR knee kinematics methods produce the same results as static methods?” In: *Magnetic Resonance in Medicine* 69.6, pp. 1634–1644. ISSN: 0740-3194, 1522-2594. DOI: [10.1002/mrm.24425](https://doi.org/10.1002/mrm.24425).
- Dai, Zhen-Zhen et al. (Jan. 2021). “Comparing the Tibial Tuberosity–Trochlear Groove Distance Between CT and MRI in Skeletally Immature Patients With and Without Patellar Instability”. en. In: *Orthopaedic Journal of Sports Medicine* 9.1, p. 232596712097366. ISSN: 2325-9671, 2325-9671. DOI: [10.1177/2325967120973665](https://doi.org/10.1177/2325967120973665). URL: <http://journals.sagepub.com/doi/10.1177/2325967120973665> (visited on 05/17/2024).
- Dalley, Arthur F., A. M. R. Agur, and Keith L. Moore (2023). *Moore’s clinically oriented anatomy*. Ninth edition. Philadelphia: Wolters Kluwer. 1 p. ISBN: 978-1-975154-08-0.
- Edelman, Robert R., ed. (2005). *Clinical magnetic resonance imaging*. Philadelphia, Pa.: Saunders. ISBN: 978-0-7216-0306-3.
- Egloff, C, T Hügle, and V Valderrabano (July 19, 2012). “Biomechanics and pathomechanisms of osteoarthritis”. In: *Swiss Medical Weekly*. ISSN: 1424-7860, 1424-3997. DOI: [10.4414/smw.2012.13583](https://doi.org/10.4414/smw.2012.13583).
- Haase, A et al. (Apr. 1986). “FLASH imaging. Rapid NMR imaging using low flip-angle pulses”. en. In: *Journal of Magnetic Resonance (1969)* 67.2, pp. 258–

266. ISSN: 00222364. DOI: 10 . 1016 / 0022 - 2364(86) 90433 - 6. URL: <https://linkinghub.elsevier.com/retrieve/pii/0022236486904336> (visited on 04/19/2024).
- Heidari, Behzad (2011). "Knee osteoarthritis prevalence, risk factors, pathogenesis and features: Part I". In: *Caspian Journal of Internal Medicine* 2.2, pp. 205–212. ISSN: 2008-6164.
- IQWiG (Aug. 2021). *In brief: How does the knee work?* InformedHealth.org [Internet]. Cologne, Germany: Institute for Quality and Efficiency in Health Care (IQWiG); 2006-. Updated 2021 Aug 24. URL: <https://www.ncbi.nlm.nih.gov/books/NBK561512/>.
- Jeon, Jeongwoo et al. (June 23, 2020). *Alteration of Screw-home Movement in Patients With Knee Osteoarthritis: A Cross-sectional Study*. DOI: 10.21203/rs.3.rs-35701/v1. URL: <https://www.researchsquare.com/article/rs-35701/v1> (visited on 05/20/2024).
- Jogi, Sandeep P. et al. (Mar. 2022). "Device for Assessing Knee Joint Dynamics During Magnetic Resonance Imaging". In: *Journal of Magnetic Resonance Imaging* 55.3, pp. 895–907. ISSN: 1053-1807, 1522-2586. DOI: 10.1002/jmri.27877. URL: <https://onlinelibrary.wiley.com/doi/10.1002/jmri.27877> (visited on 05/20/2024).
- Kijowski, R. et al. (Mar. 2020). "Osteoarthritis year in review 2019: imaging". In: *Osteoarthritis and Cartilage* 28.3, pp. 285–295. ISSN: 10634584. DOI: 10.1016/j.joca.2019.11.009. URL: <https://linkinghub.elsevier.com/retrieve/pii/S1063458419312968> (visited on 05/20/2024).
- Kim, Ha Yong et al. (Sept. 2015). "Screw-Home Movement of the Tibiofemoral Joint during Normal Gait: Three-Dimensional Analysis". In: *Clinics in Orthopedic Surgery* 7.3, pp. 303–309. ISSN: 2005-4408. DOI: 10.4055/cios.2015.7.3.303.
- Liu, Fang et al. (Apr. 2018). "Deep convolutional neural network and 3D deformable approach for tissue segmentation in musculoskeletal magnetic resonance imaging". In: *Magnetic Resonance in Medicine* 79.4, pp. 2379–2391. ISSN: 0740-3194, 1522-2594. DOI: 10.1002/mrm.26841.
- Maquet, P.G.J. (2012). *Biomechanics of the Knee: With Application to the Pathogenesis and the Surgical Treatment of Osteoarthritis*. Springer Berlin Heidelberg. ISBN: 9783642963605. URL: <https://books.google.de/books?id=pBIyBwAAQBAJ>.
- McWalter, E. J. et al. (Jan. 2005). "Use of novel interactive input devices for segmentation of articular cartilage from magnetic resonance images". In: *Osteoarthritis*

- and *Cartilage* 13.1, pp. 48–53. ISSN: 1063-4584. DOI: [10.1016/j.joca.2004.09.008](https://doi.org/10.1016/j.joca.2004.09.008).
- Menchón-Lara, Rosa-María et al. (Sept. 23, 2019). “Reconstruction techniques for cardiac cine MRI”. In: *Insights into Imaging* 10.1, p. 100. ISSN: 1869-4101. DOI: [10.1186/s13244-019-0754-2](https://doi.org/10.1186/s13244-019-0754-2).
- Myers, Casey A. et al. (Jan. 2012). “In Vivo Tibiofemoral Kinematics During 4 Functional Tasks of Increasing Demand Using Biplane Fluoroscopy”. In: *The American Journal of Sports Medicine* 40.1, pp. 170–178. ISSN: 0363-5465, 1552-3365. DOI: [10.1177/0363546511423746](https://doi.org/10.1177/0363546511423746). URL: <http://journals.sagepub.com/doi/10.1177/0363546511423746> (visited on 05/20/2024).
- Nelder, J. A. and R. Mead (Jan. 1, 1965). “A Simplex Method for Function Minimization”. In: *The Computer Journal* 7.4, pp. 308–313. ISSN: 0010-4620, 1460-2067. DOI: [10.1093/comjnl/7.4.308](https://doi.org/10.1093/comjnl/7.4.308). URL: <https://academic.oup.com/comjnl/article-lookup/doi/10.1093/comjnl/7.4.308> (visited on 05/16/2024).
- Netter, Frank H. (2023). *Netter atlas of human anatomy: classic regional approach*. Eighth edition. Philadelphia, PA: Elsevier. ISBN: 978-0-323-68042-4.
- Obermüller, Dominik et al. (Mar. 2024). “Epidemiology and treatment of pain associated with osteoarthritis of the knee in Germany: A retrospective health claims data analysis”. In: *Osteoarthritis and Cartilage Open* 6.1, p. 100430. ISSN: 26659131. DOI: [10.1016/j.ocarto.2023.100430](https://doi.org/10.1016/j.ocarto.2023.100430). URL: <https://linkinghub.elsevier.com/retrieve/pii/S2665913123000973> (visited on 03/27/2024).
- Rathnayaka, Kanchana et al. (Apr. 2012). “Quantification of the accuracy of MRI generated 3D models of long bones compared to CT generated 3D models”. en. In: *Medical Engineering & Physics* 34.3, pp. 357–363. ISSN: 13504533. DOI: [10.1016/j.medengphy.2011.07.027](https://doi.org/10.1016/j.medengphy.2011.07.027). URL: <https://linkinghub.elsevier.com/retrieve/pii/S1350453311001925> (visited on 05/15/2024).
- Rickenbach, Robert (June 11, 2013). “Optical spectrum modulated position sensor having a controller with at least one fiber optic line”. U.S. pat. 8461514B1. Individual. URL: <https://patents.google.com/patent/US8461514B1/en?oq=US-8461514-B1> (visited on 04/23/2024).
- Segal, Neil A. and Natalie A. Glass (Nov. 2011). “Is Quadriceps Muscle Weakness a Risk Factor for Incident or Progressive Knee Osteoarthritis?” In: *The Physician and Sportsmedicine* 39.4, pp. 44–50. ISSN: 0091-3847, 2326-3660. DOI: [10.3810/psm.2011.11.1938](https://doi.org/10.3810/psm.2011.11.1938). URL: <http://www.tandfonline.com/doi/full/10.3810/psm.2011.11.1938> (visited on 05/20/2024).

- Standring, Susan and Henry Gray, eds. (2021). *Gray's anatomy: the anatomical basis of clinical practice*. Forty-second edition. OCLC: on1202943188. Amsterdam: Elsevier. 1588 pp. ISBN: 978-0-7020-7705-0.
- Westbrook, Catherine and John Talbot (2019). *MRI in Practice*. Fifth Edition. Hoboken, NJ Chichester, West Sussex: Wiley Blackwell. 395 pp. ISBN: 978-1-119-39199-9.
- WHO (2023). URL: <https://www.who.int/news-room/fact-sheets/detail/osteoarthritis> (visited on 07/14/2023).
- Winkelmann, Stefanie et al. (Jan. 2007). “An Optimal Radial Profile Order Based on the Golden Ratio for Time-Resolved MRI”. en. In: *IEEE Transactions on Medical Imaging* 26.1, pp. 68–76. ISSN: 0278-0062. DOI: [10.1109/TMI.2006.885337](https://doi.org/10.1109/TMI.2006.885337). URL: <http://ieeexplore.ieee.org/document/4039540/> (visited on 04/18/2024).
- Wood, Tobias C. and contributors (2020). *Riesling: A reconstruction toolbox optimized for 3D non-cartesian MR images*. Presented at ISMRM 2020. URL: <https://github.com/spinicist/riesling>.
- Yelin, Edward, Stuart Weinstein, and Toby King (Dec. 2016). “The burden of musculoskeletal diseases in the United States”. In: *Seminars in Arthritis and Rheumatism* 46.3, pp. 259–260. ISSN: 00490172. DOI: [10.1016/j.semarthrit.2016.07.013](https://doi.org/10.1016/j.semarthrit.2016.07.013). URL: <https://linkinghub.elsevier.com/retrieve/pii/S0049017216301445> (visited on 05/20/2024).
- Zaitsev, Maxim, Julian Maclare, and Michael Herbst (Oct. 2015). “Motion artifacts in MRI: A complex problem with many partial solutions”. eng. In: *Journal of magnetic resonance imaging: JMRI* 42.4, pp. 887–901. ISSN: 1522-2586. DOI: [10.1002/jmri.24850](https://doi.org/10.1002/jmri.24850).

A Appendix

The non aggregated results for Figures 22 and 23 are shown below:

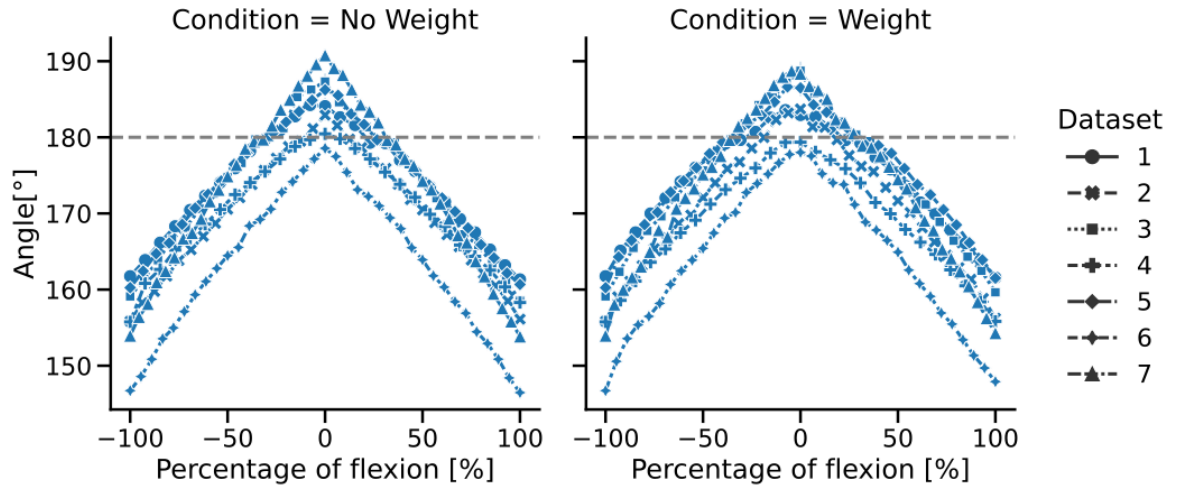


Figure 25: Non aggregated results for the angle between the long axis of the bone segments. Loaded and unloaded measurements are shown in their respective columns.

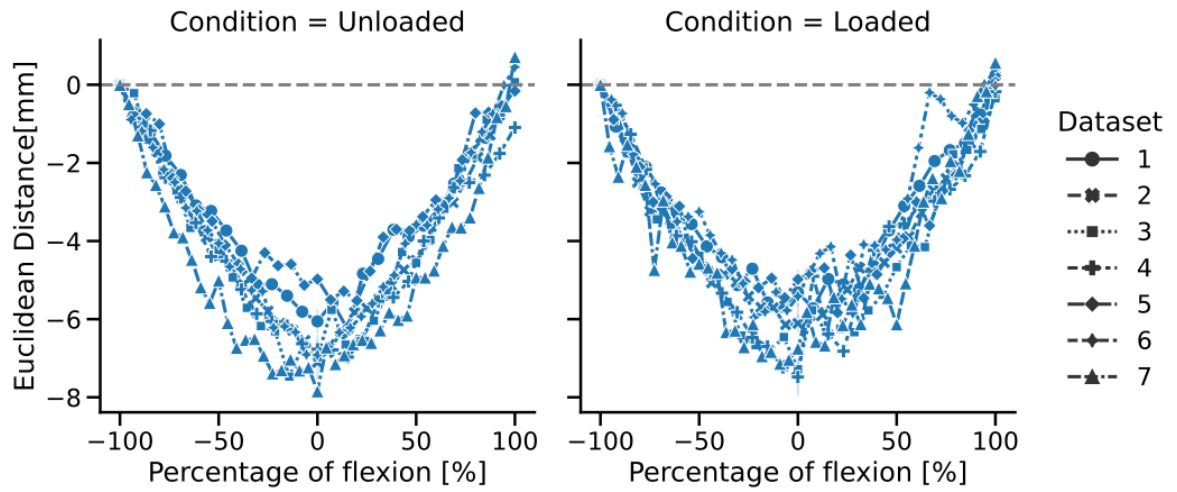


Figure 26: Non aggregated results for the euclidean distance between anatomical landmarks on the femur and tibia. Loaded and Unloaded conditions are shown in their respective columns.

Statutory Declaration:

I declare that I have developed and written the enclosed Master Thesis completely by myself, and have not used sources or means without declaration in the text. Any thoughts from others or literal quotations are clearly marked. The Master Thesis was not used in the same or in a similar version to achieve an academic grading or is being published elsewhere.

Place, Date

Signature